

1 **In-situ Observation of Riming in Mixed-Phase Clouds using the PHIPS**  
2 **probe**

3 Fritz Waitz<sup>a</sup> Martin Schnaiter<sup>a,b</sup> Thomas Leisner<sup>a</sup> Emma Järvinen<sup>a</sup>

4 <sup>a</sup> *Institute of Meteorology and Climate Research, Karlsruhe Institute of Technology, Karlsruhe,*  
5 *Germany* <sup>b</sup> *schnaiTEC GmbH, Bruchsal, Germany*

6 *Corresponding author:* Fritz Waitz, [fritz.waitz@kit.edu](mailto:fritz.waitz@kit.edu)

7 ABSTRACT: Mixed-phase clouds consist of both supercooled liquid water droplets and solid ice  
8 crystals. Despite having a significant impact on Earth's climate, mixed-phase clouds are poorly  
9 understood and not well represented in climate prediction models. One piece of the puzzle is  
10 understanding and parameterizing riming of mixed-phase cloud ice crystals, which is one of the  
11 main growth mechanisms of ice crystals via the accretion of small, supercooled droplets. Especially  
12 the extent of riming on ice crystals smaller than  $500\ \mu\text{m}$  is often overlooked in studies - mainly  
13 because observations are scarce. Here, we investigated riming in mixed-phase clouds during three  
14 airborne campaigns in the Arctic, the Southern Ocean and US east coast. Riming was observed  
15 from stereo-microscopic cloud particle images recorded with the Particle Habit Imaging and Polar  
16 Scattering (PHIPS) probe. We show that riming is most prevalent at temperatures around  $-7^\circ\text{C}$ ,  
17 where, on average, 43% of the investigated particles in a size range from  $100 \leq D \leq 700\ \mu\text{m}$  showed  
18 evidence of riming. We discuss the occurrence and properties of rimed ice particles and show  
19 correlation of the occurrence and the amount of riming with ambient microphysical parameters.  
20 We show that riming fraction increases with ice particle size ( $<20\%$  for  $D \leq 200\ \mu\text{m}$ , 35-40% for  
21  $D \geq 400\ \mu\text{m}$ ) and liquid water content (25% for  $\text{LWC} \leq 0.05\ \text{g m}^{-3}$ , up to 60% for  $\text{LWC} = 0.5\ \text{g m}^{-3}$ ).  
22 We investigate the ageing of rimed particles and the difference between "normal" and "epitaxial"  
23 riming based on a case study.

## 24 1. Introduction

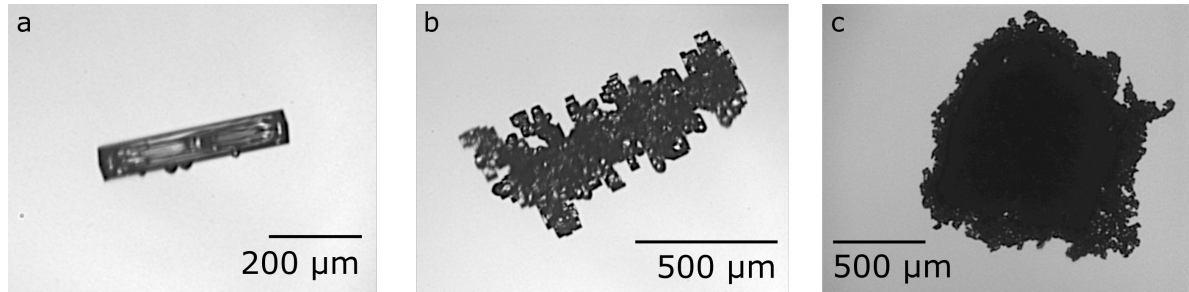
25 Mixed-phase clouds (MPCs), consisting of both supercooled liquid droplets and ice particles,  
26 play a major role in the atmospheric hydrological cycle and the radiative balance of the Earth (e.g.  
27 Korolev et al. 2017). Despite their widespread occurrence, mixed-phase cloud processes are still  
28 rather poorly understood and represent a great source of uncertainty for climate predictions (e.g.  
29 McCoy et al. 2016).

30 One important microphysical process in MPCs is *riming*, i.e. the accretion of small supercooled  
31 liquid droplets on the surface of ice particles (see example in Fig. 1a). Besides vapor deposition  
32 and aggregation, it is one of the three main ice growth modes. Riming can be divided into two  
33 (not always easily distinguishable) sub-topics: riming of small ice particles (diameter  $D \approx 100$ -  
34  $1000 \mu\text{m}$ ) in clouds and riming of large ( $1000 \lesssim D \lesssim 5000 \mu\text{m}$ ) precipitating ice, graupel, snow  
35 particles or frozen precipitation size droplets that collect smaller cloud droplets or slower falling  
36 ice particles (e.g. "*ice lollies*" (Keppas et al. 2017)). Whereas most recent publications focus  
37 on the latter aspect (riming of large precipitating particles), in this study, we focus on riming of  
38 smaller ice particles in clouds.

39 The typical life-cycle of an exemplary rimed particle is usually as follows: The ice particle is  
40 formed, followed by growth via vapor deposition until the particle has reached a critical minimum  
41 size for riming (depending on shape and habit, e.g.  $D \geq 60 \mu\text{m}$  for columns, (e.g. Ono 1969;  
42 Ávila et al. 2009)). If liquid droplets are present in large enough numbers, the ice particle starts  
43 collecting supercooled droplets (around  $D = 10 - 40 \mu\text{m}$ , e.g. Harimaya (1975)) that freeze on  
44 the particle's surface. When the ice particles have acquired enough mass so gravitational settling  
45 becomes efficient, they precipitate and accrete even more droplets whilst falling and grow further  
46 until it reaches the ground as graupel.

47 Ice particle growth, both in size and mass, can ultimately change cloud lifetime and radiative  
48 properties. The scavenging of supercooled liquid water affects droplet size distribution and number  
49 concentration and thus liquid water content as well as aerosol concentration (Baltensperger et al.  
50 1998; Hegg et al. 2011). Also, splintering during the riming process can initiate secondary ice  
51 formation, thus leading to the formation of new ice particles known as the *Hallett-Mossop-process*  
52 (e.g. Hallett and Mossop 1974; Korolev et al. 2020; Field et al. 2017). Since rimed ice particles  
53 are of higher mass and more compact compared to unrimed particles, their fall speed and terminal

54 velocity are increased (Locatelli and Hobbs 1974; Lin et al. 2011; Garrett and Yuter 2014).  
 55 Furthermore, riming leads to increased surface roughness and complexity, and hence affects the  
 56 ice particles' radiative properties, as shown in e.g. Schnaiter et al. (2016); Järvinen et al. (2018);  
 57 Järvinen et al. (2021).



58 FIG. 1. Example of a (a) slight "normally" rimed , (b) heavily "epitaxially" rimed column and (c) a graupel  
 59 particle captured by the PHIPS probe during the IMPACTS campaign.

60 In principle, riming can occur everywhere where ice particles and supercooled droplets coexist.  
 61 Pflaum and Pruppacher (1979) have defined the collection kernel of a collector with radius  $R$  and  
 62 a droplet with radius  $r$  that have a relative velocity  $\Delta v$  against each other as

$$K = E_1 E_2 \pi (r + R)^2 \Delta v \quad (1)$$

63 where  $E_1$  is the collision efficiency of the two particles and  $E_2$  the efficiency that the two particles  
 64 remain attached to each other. Ice-ice collisions can lead to aggregation, droplet-droplet collisions  
 65 to coalescence and ice-droplet collisions to riming. For riming, these quantities depend on numer-  
 66 ous parameters including temperature (Kneifel and Moisseev 2020), humidity (Khain et al. 1999),  
 67 habit, size and orientation of the ice particle (Ono 1969; Wang and Ji 2000; Ávila et al. 2009),  
 68 number and size distribution of the supercooled droplets (Saleeby and Cotton 2008) as well as  
 69 turbulence and vertical velocity (Herzogh and Hobbs 1980; Garrett and Yuter 2014). The number  
 70 of rime on an ice particle is hence dependent on all these quantities throughout particle's trajectory  
 71 in the cloud and during precipitation.

72 In recent years, multiple studies have used radar measurements to retrieve information about  
 73 snow and riming density based on their vertical Doppler velocity (Mosimann et al. 1993; Leinonen  
 74 and Szyrmer 2015; Leinonen et al. 2018; Mason et al. 2018; Kneifel and Moisseev 2020). Those



75 methods proved to be fit to determine the riming state (i.e. whether a particle is rimed or unrimed)  
76 of large, precipitating snow and graupel particles. However, they cannot resolve the fine structure  
77 of small or freshly rimed ice particles inside clouds if the radar signal is dominated by large graupel  
78 particles in the size range  $D = 1 - 10$  mm. In-situ studies with high-resolution cloud imaging probes  
79 investigating the properties of individual rimed particles sampled directly in the cloud, however, are  
80 scarce. The difficulty is to resolve riming features and discriminate between rimed and non-rimed  
81 irregular particles. Furthermore, analysis of particle images is quite complex and hence automate  
82 and manual assessment of particle properties is very laborious. Consequently, the riming of ice  
83 particles is often times poorly or not at all represented in climate prediction models. So far, the  
84 exact processes influencing the riming of cloud particles are not well understood. A deterministic  
85 parameterization of when and where to expect how much riming does not exist. Most models  
86 account for the riming degree (i.e. what fraction of a crystal's surface is covered by rime) only  
87 in the sense of a *subtype* for hydrometeors (e.g. *cloud ice*, *graupel*, *snow*, COSMO, Blahak and  
88 Seifert (2015), <http://www.cosmo-model.org/>). Furthermore, riming is neglected completely in  
89 most Arctic model studies (e.g. Fan et al. 2011; Ovchinnikov et al. 2014; Stevens et al. 2018).

90 In this work, we investigate riming of ice particles using the Particle Habit Imaging and Polar  
91 Scattering (PHIPS) probe. PHIPS is an aircraft-mounted cloud probe acquiring stereo-microscopic  
92 images and corresponding angular scattering functions of single cloud particles in the size range  
93  $D = 20 - 700 \mu\text{m}$  and  $D = 50 - 700 \mu\text{m}$  for ice and droplets, respectively. With its high optical  
94 resolution and single particle measurements, PHIPS is well suited to investigate detailed features  
95 like riming of individual ice particles. We present microphysical observations of ice particles  
96 from three field campaigns investigating high latitude MPC. In section 2, we give an overview  
97 of the three field campaigns as well as a brief introduction of the PHIPS probe and its data  
98 analysis methods. Combining the data from these three field campaigns, an extensive data-set  
99 observing ice particles of various size, habit and riming state has been acquired. In section 3,  
100 we present a statistical analysis of the correlation with ambient conditions of rimed particles for  
101 different degrees of riming. We estimate the minimum size of rimed particles as well as droplets,  
102 confirming the results of previous laboratory studies. Further, we highlight various riming features  
103 such as one-sided rimed plates or "*ice lollies*". One particularly interesting observation is ice  
104 particles carrying small, faceted rime oriented to the crystalline axis of the host particle. Such

105 particles have been observed before (Korolev et al. 2020) but their occurrence and properties have  
106 not been studied comprehensively. This type of riming, which we call *Epitaxial Riming* and which  
107 is e.g. shown in Fig. 1b, will be analyzed in detail in section 4 including a case study showing the  
108 typical step-by-step evolution of epitaxially rimed particles.

## 109 **2. Methods and Experimental Data Set**

### 110 *a. Campaigns*

111 In this work, we use experimental in-situ data gathered during three airborne field campaigns:

- 112 1. ACLOUD - Arctic CLOUD Observations Using airborne measurements during polar Day,  
113 May/June 2017 based in Svalbard (Spitsbergen, Norway) with the AWI Polar6 aircraft  
114 ( 165 flight hours),
- 115 2. SOCRATES - Southern Ocean Clouds, Radiation, Aerosol Transport Experimental Study,  
116 Jan/Feb 2018 based in Hobart (Tasmania, Australia) with the NCAR Gulfstream-V aircraft  
117 ( 105 flight hours) and
- 118 3. IMPACTS - Investigation of Microphysics and Precipitation for Atlantic Coast-Threatening  
119 Snowstorms, Jan/Feb 2020 based in Wallops (VA, USA) with the NASA P3 aircraft ( 53 flight  
120 hours).

121 An overview of the microphysical conditions as well as the instrumentation during those cam-  
122 paigns can be found in Knudsen et al. (2018) and Wendisch et al. (2019) for ACLOUD, McFarquhar  
123 et al. (2019) for SOCRATES and McMurdie et al. (2019) for IMPACTS. The sampling during those  
124 three campaigns includes a wide variety of different cloud conditions: warm clouds, supercooled  
125 liquid clouds, ice clouds and mixed-phase clouds. Clouds sampled ranged in altitude from bound-  
126 ary layer clouds below 200 m to mid-level clouds between 4000 m and 6000 m asl. Temperatures  
127 ranged from -20 to +5°C during ACLOUD, -35 to +5°C during SOCRATES and -32 to +9°C  
128 during IMPACTS. The sampled ice particles covered a wide range of different particle shapes  
129 and habits (columns, plates, needles, bullet rosettes, dendrites and irregulars, including rough,  
130 rimed and pristine particles) as well as sizes from  $D = 20 - 700 \mu\text{m}$ . The instrumentation on the  
131 three aircraft included cloud particles probes such as the SID-3 (*Small Ice Detector Mk. 3*), CDP  
132 (*Cloud Droplet Probe*, DMT, Longmont, USA), CIP (*Cloud Imaging Probe*, DMT, Longmont,

133 USA) and PIP (*Precipitation Imaging Probe*, DMT, Longmont, USA) during ACLOUD, 2D-C,  
134 2D-S (*Two-dimensional Stereo Probe, Two-dimensional Cloud Probe*, SPEC Inc., Boulder, USA)  
135 and CDP during SOCRATES and 2D-S, CDP and CPI (*Cloud Particle Imager*, SPECinc, Boulder,  
136 CO, USA) during IMPACTS.

137 For SOCRATES, vertical Doppler velocity was measured by the HCR (HIAPER cloud Radar,  
138 UCAR/NCAR-EOL (2022)) which has a transmit frequency 94.40 GHz (W-band), temporal reso-  
139 lution 10 Hz, vertical range resolution of 20 to 180 m and a typical radial velocity uncertainty of  
140  $0.2 \text{ m s}^{-1}$  at a vertical velocity of  $w = 2 \text{ m s}^{-1}$ ). The velocity data is corrected for aircraft motion and  
141 aliasing-bias. The ambient temperature was measured with a heated temperature sensor (Harco  
142 149 Model 100009-1 Deiced TAT) that has a general accuracy of  $0.3^\circ\text{C}$ . The vertical velocity  
143 was measured using a Radome air-motion system (UCAR/NCAR-Earth Observing Laboratory  
144 2019). Relative humidity was measured by the VCSEL (Vertical-Cavity Surface-Emitting Laser  
145 hygrometer) with an uncertainty ranging from 6% to 10% (Diao 2021). During ACLOUD, the  
146 temperature was measured using an open-wire Pt100 in an unheated Rosemount housing at the tip  
147 of the noseboom with a frequency of 100 Hz and an estimated accuracy of  $\pm 0.1^\circ\text{C}$ . The vertical  
148 wind was measured using a Rosemount 858 five-hole probe with a relative accuracy of the vertical  
149 wind speed of  $\pm 0.05 \text{ m/s}$  for straight and level flight sections. During IMPACTS, atmospheric state  
150 measurements were performed using the Rosemount Total Air Temperature (TAT) probe and the  
151 Edgetech three-stage chilled mirror hygrometer with 1 Hz temporal resolution (Martin and Bennett  
152 2020). For each PHIPS particle, the corresponding temperature, humidity and velocity data as well  
153 as LWC were determined as the average over  $t = t_s \pm 0.5 \text{ s}$  around the time of acquisition  $t_s$  where  
154 each PHIPS particle was sampled.

155 Due to the variability of the microphysical conditions and sampled particles, the data gathered  
156 during these three campaigns provide a suitable and representative data set for a comprehensive  
157 characterization of riming in mixed-phase clouds. All data cited in this work can be found in the  
158 corresponding data bases for the three campaigns: Ehrlich et al. (2019) for ACLOUD, EOL (2018)  
159 for SOCRATES, McMurdie et al. (2019) for IMPACTS.

160 *b. The PHIPS Probe*

161 PHIPS is designed to investigate the microphysical and light scattering properties of cloud par-  
162 ticles. It produces microscopic stereo-images whilst simultaneously measuring the corresponding  
163 angular scattering function for the angular range from  $18^\circ$  to  $170^\circ$  for single cloud particles. More  
164 information and a detailed characterization of the PHIPS setup and instrument properties can be  
165 found in depth in Abdelmonem et al. (2016) and Schnaiter et al. (2018). From the stereo images,  
166 single-particle microphysical features such as e.g. area equivalent diameter or aspect ratio, can  
167 be obtained. The image analysis algorithm is explained in depth in Schön et al. (2011). Based  
168 on the single-particle's angular scattering function, the thermodynamic phase and the scattering  
169 equivalent diameter can be derived as explained in Waitz et al. (2021).

170 For ALOUD and SOCRATES, the instrument settings were set to measure single cloud particles  
171 in a size range from  $50 \mu\text{m} \leq D \leq 700 \mu\text{m}$  and  $20 \mu\text{m} \leq D \leq 700 \mu\text{m}$  for droplets and ice particles,  
172 respectively. The image acquisition rate of the microscopic system was limited to 3 Hz in these  
173 campaigns, while single-particle scattering data could be acquired up to a maximum rate of 3.5 kHz.  
174 The magnification settings of the cameras corresponded to an optical resolution of approximately  
175  $3.3 \mu\text{m}$ . Since PHIPS characterizes individual particles, it has a narrow sensitive area ( $A_{\text{sens}}$ ). As  
176 discussed in Waitz et al. (2021),  $A_{\text{sens}}$  is size dependent (e.g.  $A_{\text{sens}} = 0.5 \text{ mm}^2$  for ice particles with  
177  $D = 200 \mu\text{m}$ ). Assuming a relative flight speed of  $v_s = 150 \text{ m s}^{-1}$ , this corresponds to a sampling  
178 volume of  $V_{\text{sens}} = A_{\text{sens}} \cdot v_s = 0.08 \text{ L s}^{-1}$ . During IMPACTS, the scientific focus was on larger ice  
179 crystals so the trigger threshold as well as the magnification were increased to trigger only particles  
180 larger than  $D \geq 100 \mu\text{m}$  for droplets and  $D \geq 40 \mu\text{m}$  for ice. The magnification settings of the  
181 cameras corresponded to an optical resolution of approximately  $4 \mu\text{m}$  and the maximum camera  
182 acquisition rate was varied between 3 to 10 Hz, which corresponds to a maximum spatial resolution  
183 of roughly one stereo-image per 15 m.

184 *c. Manual Image Classification*

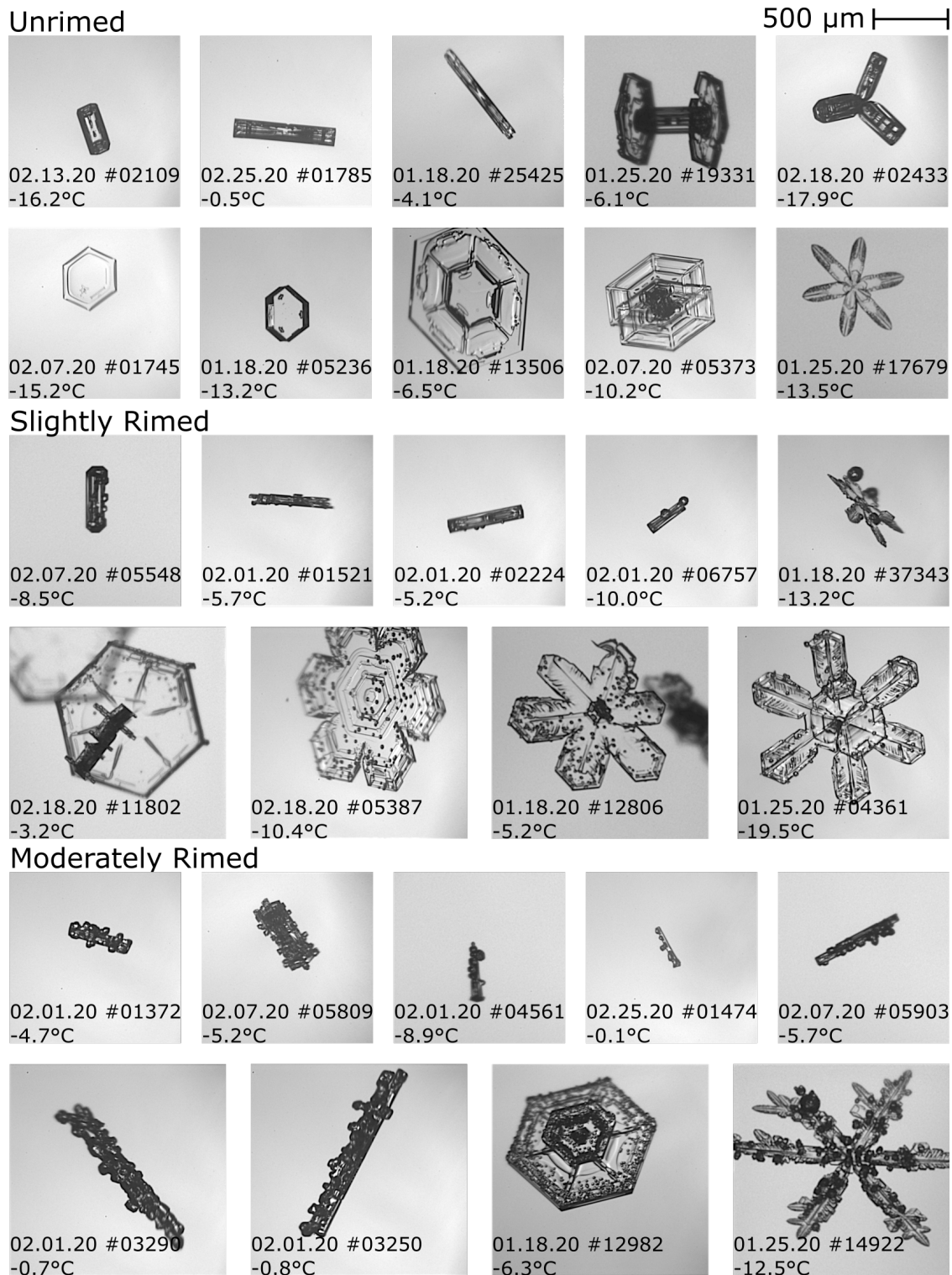
185 All PHIPS stereo-images from the ALOUD and SOCRATES data-set were visually classified  
186 into seven habit classes: (i) plate-like particles (single plates, sectorized plates, skeleton plates and  
187 side planes), (ii) columnar particles (solid columns, hollow columns and sheaths), (iii) needles,  
188 (iv) frozen droplets, (v) bullet rosettes, (vi) graupel, and (vii) irregular particles. In addition to the

189 habits, the particles were assigned the attributes *rimed* or *unrimed*. The temperature dependent  
190 frequency of occurrence distribution of the different particle habits are shown in the SI (Fig. S1).  
191 An overview of the riming fraction and riming type (normal, epitaxial, see Sec. 4) per habit is  
192 shown in Fig. S2.

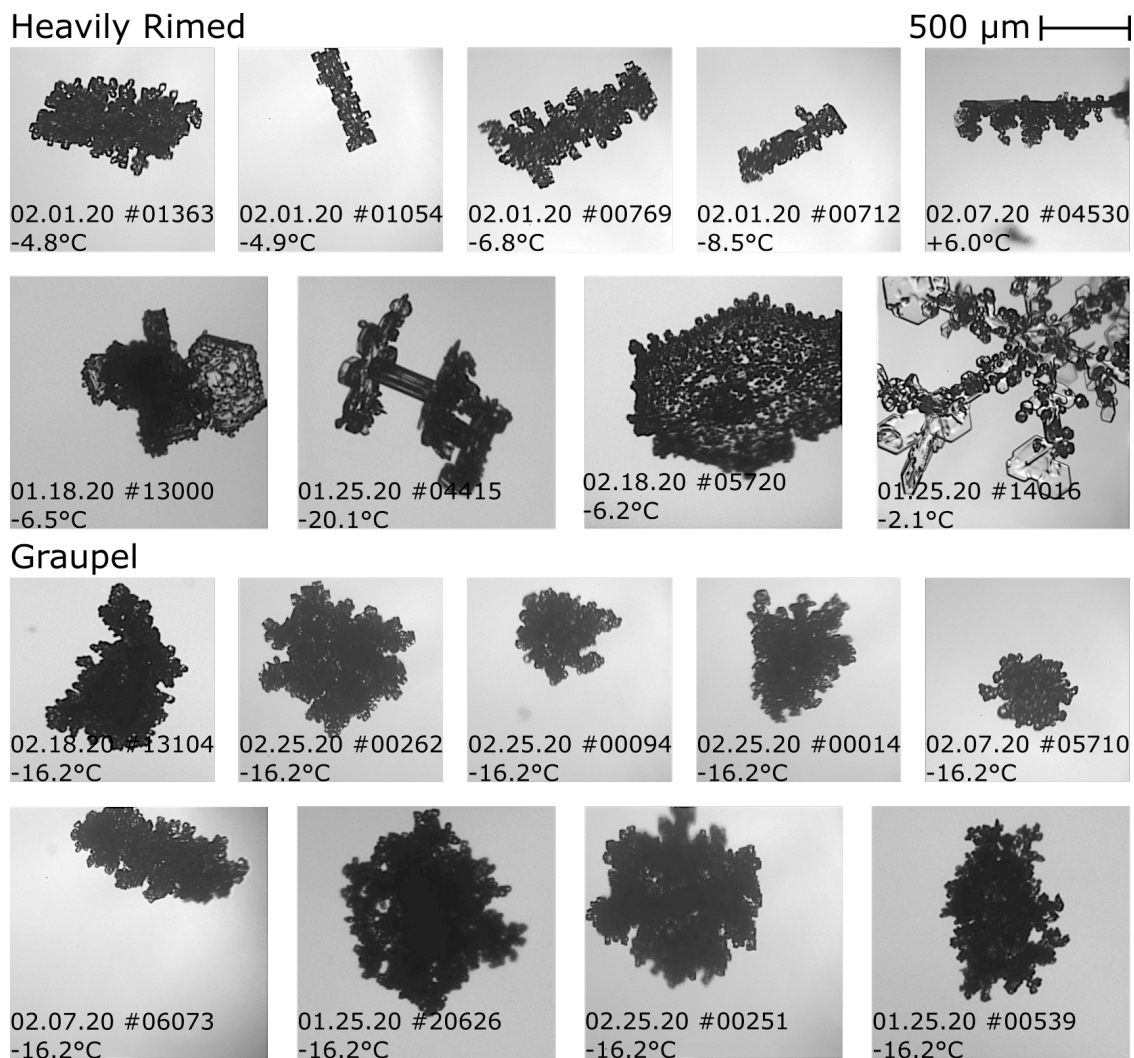
193 In a next classification step, a subset of the well classified particles was again visually classified  
194 further regarding their riming features. The second classification step was performed only for  
195 particles larger than 100  $\mu\text{m}$  sampled at a temperature  $T \geq -17^\circ\text{C}$ . Smaller particles were almost  
196 exclusively small irregulars whose riming state could not be classified with certainty due to the  
197 limited optical resolution and almost no riming was observed at lower temperatures, see Fig. 4a.  
198 CDP LWC ranged from 0  $\text{g}/\text{m}^3$  to 0.5  $\text{g}/\text{m}^3$  and vertical HCR Doppler velocity from -4  $\text{m}/\text{s}$  to  
199 +2  $\text{m}/\text{s}$ .

200 Particles were classified regarding their surface riming degree (SRD) as (i) unrimed (SRD = 0%,  
201 no visible riming on any of the two stereo-micrographs), (ii) slightly rimed (SRD < 25%, a few  
202 scattered rime particles on the crystal's surface), (iii) moderately rimed (25%  $\leq$  SRD  $\leq$  50%, up to  
203 half of the particle's surface is covered by rime), (iv) heavily rimed (50% < SRD < 100%, most of  
204 the particle's surface is covered by rime) as well as (v) graupel (SRD = 100%, the whole particle  
205 surface is covered by multiple layers of rime, so that the structure of the underlying particle is no  
206 longer recognizable). Exemplary PHIPS particles from these classes are shown in Figs. 2 and 3.  
207 This classification approach is similar to the definition of riming degree used in previous studies  
208 such as Magono and Lee (e.g. 1966); Brientjes et al. (e.g. 1987); Mosimann et al. (e.g. 1993,  
209 1994); Mosimann (e.g. 1995). Also, the attributes (i) one-sided riming and (ii) epitaxial riming  
210 (which will be explained in detail in section 4) were assigned. As each particle is imaged from two  
211 different viewing angles (120° apart), whether or not a particle has rime only on one side can also  
212 be assessed for opaque particles (see examples in Fig. 6).

213 The remaining data-set includes 3,957 particles from ALOUD and 1,413 from SOCRATES.  
214 Examples of particles classified in the different categories are shown in the following section.  
215 Manual classification was not applied for the complete IMPACTS data set due to large number of  
216 ice particle images (over 250,000 images were acquired). Therefore, only the set of images used  
217 for the case study presented in section b was manually inspected.



218 FIG. 2. Examples of representative PHIPS particles with different degrees of riming categorized by the  
 219 surface riming degree (SRD): unrimed (SRD = 0%), slightly rimed (0% < SRD < 25%) and moderately rimmed  
 220 (25 ≤ SRD ≤ 50%) particles. Heavily rimed (50% < SRD < 100%) and graupel particles (SRD = 100%) are  
 221 shown in Fig. 3.



222 FIG. 3. Examples of representative PHIPS particles with different degrees of riming depending on the surface  
 223 riming degree (SRD): heavily rimed ( $50\% < \text{SRD} < 100\%$ ) and graupel particles ( $\text{SRD} = 100\%$ ). Unrimed  
 224 ( $\text{SRD} = 0\%$ ), slightly rimed ( $0\% < \text{SRD} < 25\%$ ) and moderately rimed particles ( $25 \leq \text{SRD} \leq 50\%$ ) are shown  
 225 in Fig. 2.

### 226 3. Statistical Analysis and Correlation with Ambient Conditions

227 As discussed in the introduction, riming is dependent on a variety of atmospheric quantities  
 228 including temperature, humidity and vertical wind velocity as well as trajectory and microphysical  
 229 properties such as number concentration, size distribution, habit and orientation of ice particles  
 230 and supercooled droplets. It is not possible to know each of those parameters for each particle  
 231 at every given moment. Hence, as already mentioned above, such detailed description of riming

232 on a particle-by-particle basis is not present in current climate prediction models and riming  
233 is only accounted for in terms of graupel and snow and rarely for smaller, less densely rimed  
234 particles. Here, we investigate riming of sub-millimeter ice particles based on in situ aircraft data  
235 and correlate the relative occurrence of rimed and unrimed ice particles with other microphysical  
236 parameters. Note that the measured conditions do not necessarily represent the environment where  
237 the particles experienced riming but rather where they were sampled. This statistic is based on  
238 5,370 manually classified images from the ACLOUD and SOCRATES campaign.

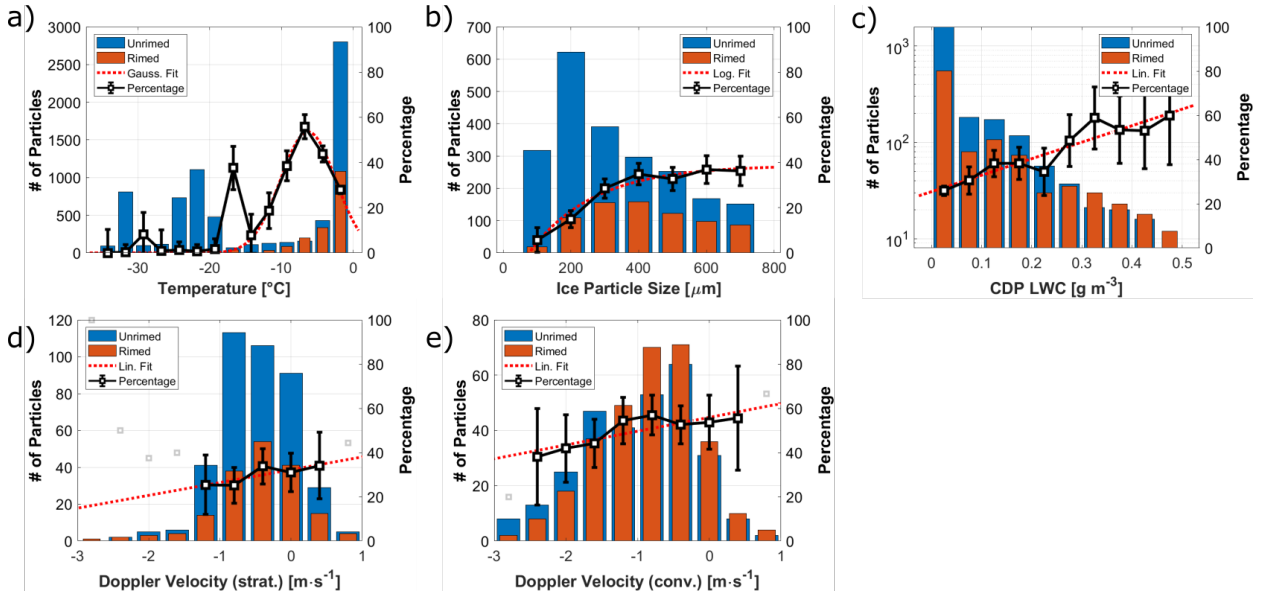
### 239 *a. Riming Fraction*

240 In the following, "riming fraction" refers to the relative amount of rimed particles compared to  
241 total amount of classified ice particles (rimed + unrimed). Fig. 4a shows the correlation of riming  
242 fraction and ambient temperature. The corresponding fit parameters for all histograms are shown  
243 in Table 1. Most riming was observed in a temperature range between  $-10^{\circ}\text{C} \leq T \leq 0^{\circ}\text{C}$  with the  
244 maximum around  $T \simeq -7^{\circ}\text{C}$  where up to 55% of all ice particles were rimed. The high riming  
245 fraction around  $-17^{\circ}\text{C}$  is due to a very high rimed fraction in this temperature bin during a single  
246 cloud segment of RF09 of SOCRATES. It is based on a low number of total particles ( $n = 213$ )  
247 and is therefore not assumed to be a generalizable feature.

258 For the following analysis, apart from Fig. 4a, only particles sampled at  $T \geq -17^{\circ}\text{C}$  are considered.  
259 Fig. 4b shows riming statistics as a function of ice particle's area equivalent diameter retrieved from  
260 the stereo-microscopic images. It can be seen that the percentage of rimed particles increases with  
261 particle size. The riming fraction increases from below 5% for particles smaller than  $D_{\text{im,A}} \leq$   
262  $150\ \mu\text{m}$  to over 35% for particles larger than  $D_{\text{im,A}} \geq 400\ \mu\text{m}$ . Above that, the riming fraction  
263 is only weakly dependent on particle size. The smallest ice particle where riming was observed  
264 was a column with an area equivalent diameter of  $D_{\text{im,A}} = 116.1\ \mu\text{m}$  and maximum dimension  
265  $D_{\text{im,max}} = 193.7\ \mu\text{m}$  (shown in Fig. S7 in the SI). This is a larger riming onset size compared to  
266 e.g. Ono (1969); Ávila et al. (2009)) who reported a critical minimum diameter of  $D \geq 60\ \mu\text{m}$  for  
267 riming on columns collected via glass slides and analyzed by optical microscopy.

268 The correlation of riming fraction and cloud liquid water content (LWC) measured by the CDP is  
269 shown in Fig. 4c. The riming fraction increases from 25% in cloud segments with low LWC below  
270  $0.05\ \text{g m}^{-3}$  to 60% for  $\text{LWC} \geq 0.5\ \text{g m}^{-3}$ . Rime particles had a size around roughly  $D_{\text{max}} \simeq 20$  and





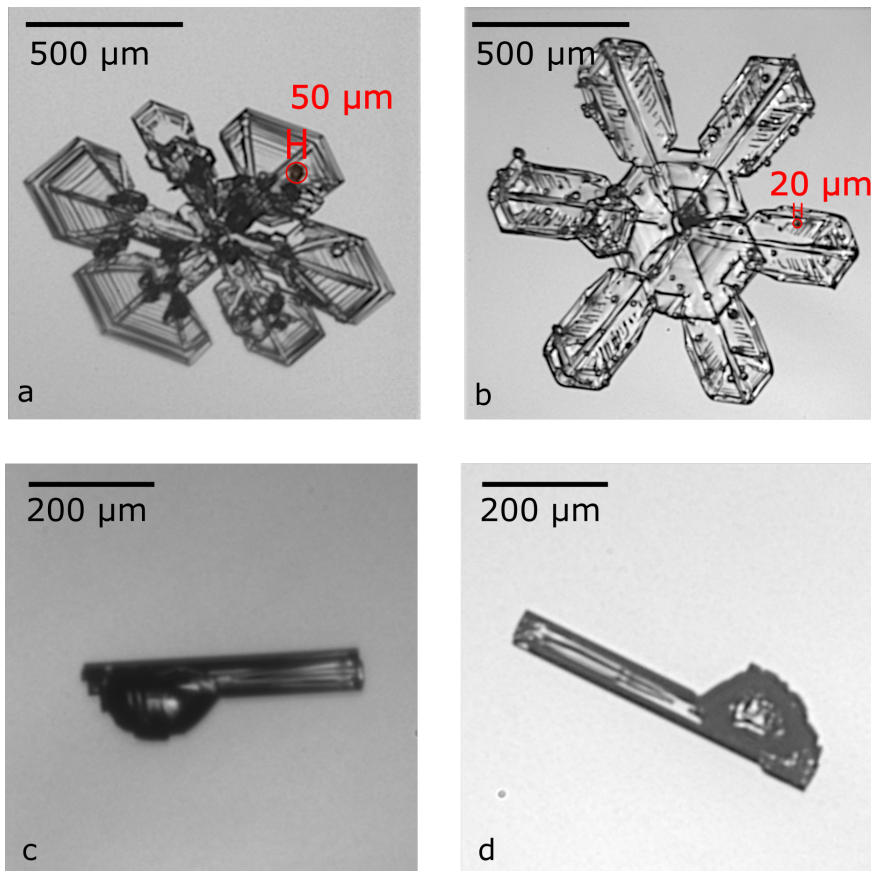
248 FIG. 4. Histograms showing the absolute number of classified unrimed (blue) and rimed (red) particles during  
 249 ACLOUD and SOCRATES as well as the riming fraction (relative percentage  $n_{\text{rimed}}/n_{\text{all}}$ , black, right axis) in  
 250 correlation with different ambient parameters: Temperature (a), area-eq. diameter of the underlying ice particle  
 251 measured by PHIPS (b), CDP liquid water content (c) and vertical HCR Doppler velocity in stratiform (d) and  
 252 convective clouds (e). HCR data is only available for SOCRATES. The red dotted line shows a fit to the riming  
 253 fraction (right y-axis). The corresponding fit parameters for all histograms are shown in Tab. 1. The statistical  
 254 uncertainty bars correspond to the number of particles per bin ( $n^{-1/2}$ ). Only bins with  $n \geq 20$  are considered for  
 255 the fit, others are shown in grey. Correlation plots with further parameters (CDP mean droplet diameter, ambient  
 256 vertical velocity, relative cloud height, relative humidity), which show only a weak dependency, are shown in  
 257 Fig. S3 in the SI.

TABLE 1. Fit parameters to the riming percentage histograms shown in Fig. 4.

		Fit function	$R^2$
Temperature		$y = -0.952 x^2 - 12.2 x + 11.9$	0.940
Ice particle diameter	(PHIPS)	$y = 38.7 - \exp[-52.8 (x-769)]$	0.964
Liquid water content	(CDP)	$y = 74.7 x + 25.5$	0.863
Vertical Doppler velocity	(HCR, strat.)	$y = 5.79 x + 32.2$	0.707
Vertical Doppler velocity	(HCR, conv.)	$y = 6.24 x + 55.9$	0.724

271 50  $\mu\text{m}$  as shown in Figs. 5a,b for two exemplary ice crystals that were amongst the crystals with the  
 272 smallest and largest rime particles based on visual inspection. This is in agreement with results  
 273 presented by e.g. Kikuchi and Uyeda (1979); Harimaya (1975), who reported sizes of rime particles

274 between 10 and 60  $\mu\text{m}$ . As there exists no automated method to determine the size of the rime  
275 particles based on the PHIPS images, the size of rime particles is not further investigated in this  
276 work. Comparison with CDP mean droplet diameter showed a slight correlation with a maximum  
277 riming fraction at  $D_{\text{drop, mean}} = 20 \mu\text{m}$  (see Fig. S3f in the SI). Figs. 5c,d show drizzle-rimed ice (*ice*  
278 *lollies*). Such contact freezing of relatively large droplets compared to the size of ice particle was  
279 reported by (Uyeda and Kikuchi 1978; Keppas et al. 2017). We also see this in our data set, but  
280 there are only very few cases. Due to the low number, no correlation with sampled PHIPS drizzle  
281 droplet concentration was found and no detailed statistical analysis was conducted.

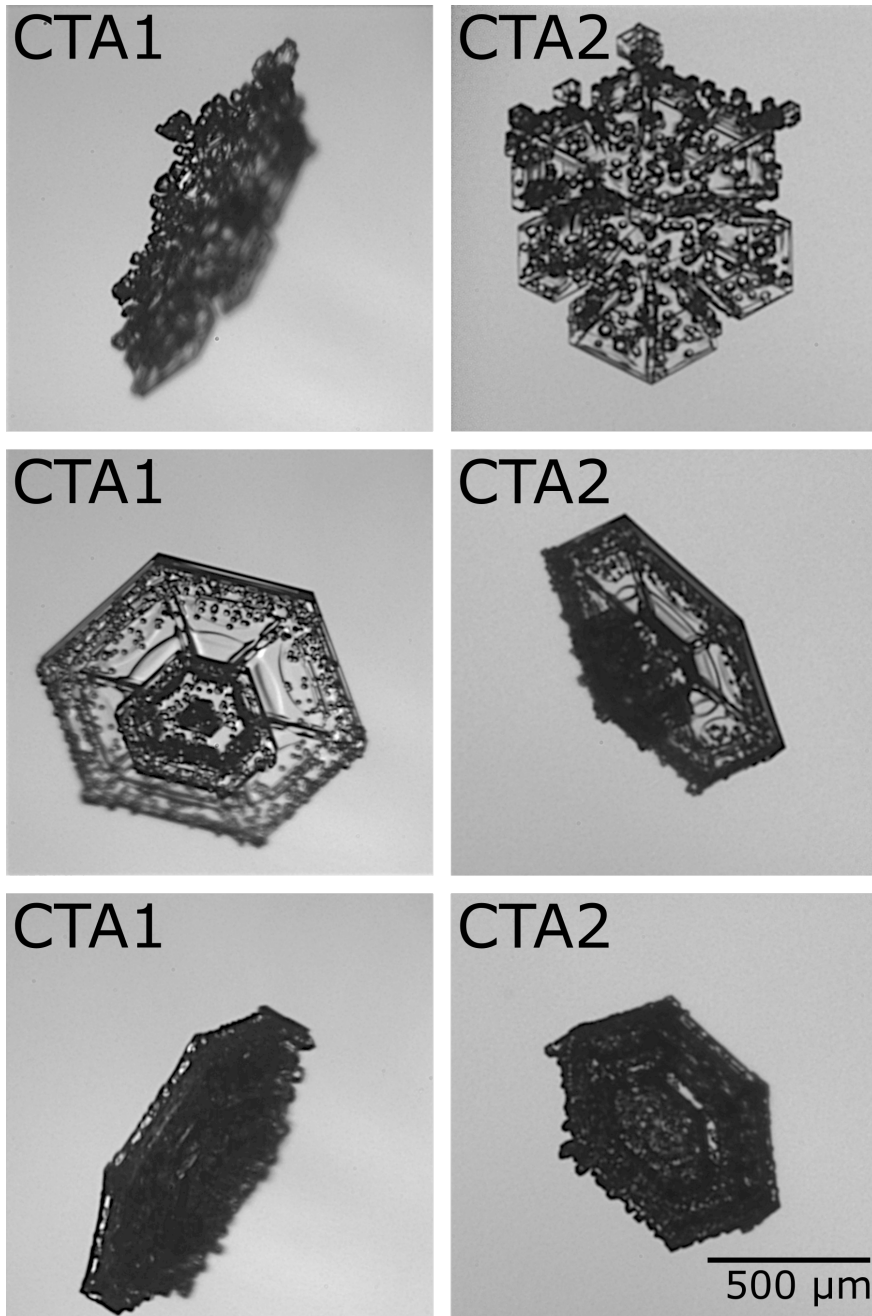


282 FIG. 5. Exemplary slightly rimed particles showing the size of rime particles on the surface (a, b) and  
283 rimed ice (ice lollies, c,d).

284 Fig. 4d and e show the correlation with the Doppler radial velocity measured by the HCR, which  
285 is the sum of vertical air velocity and particle fall speed, corrected by the vertical motion of the  
286 aircraft. HCR data are only available for the SOCRATES campaign. Since the HCR has a dead

287 zone of 145 m around the aircraft in which data are not usable, there is no data available at the  
288 location of the aircraft. Hence, each data point corresponds to the measured HCR Doppler velocity  
289 of the first valid gate closest to the aircraft. The HCR was typically rotated to point in zenith  
290 direction when flying beneath clouds or ascending through boundary layer clouds and nadir at  
291 other times. The sign was adjusted based on HCR orientation so that negative velocity always  
292 corresponds to downward direction, positive to upward direction. The analysis was divided into  
293 stratiform and convective cloud segments based on the flag given in UCAR/NCAR-EOL (2022).  
294 For stratiform cases, events for which the melting layer was close to the position of the aircraft  
295 were omitted, since events where in-situ probes and the first gate were not "on the same side" of  
296 the melting layer would lead to potentially biased velocities due to the discontinuity at the melting  
297 layer (Romatschke 2021; Romatschke and Dixon 2022). It can be seen that there is a clear trend of  
298 increasing riming fraction towards more positive (upward) Doppler velocities. Further, on average,  
299 the riming fraction is much higher in convective (52%) compared to stratiform clouds (34%). This  
300 can be explained by updrafts and in-cloud turbulence which increases the time and trajectory that  
301 the particles remain in the cloud as well as the relative velocity of ice particles against droplets and  
302 thus increases the probability that they collide to form riming.

303 The measurement of ambient vertical velocity around the aircraft shows a slight correlation  
304 towards both higher positive and negative values (see Fig. S3h in the SI). This could indicate a  
305 correlation with turbulent air motion, as riming is expected to be more likely if particles remain  
306 longer in the cloud, having a longer total travel path and hence a higher chance of collecting  
307 droplets. However, at the same time, a lot of one-sided rimed plates were observed during the  
308 campaigns (see Fig. 6), which would be unlikely if all riming would necessarily be correlated with  
309 turbulent air motion. This confirms observations of fallen snow by Ono (1969); Rango et al. (2003).  
310 Note that the ambient vertical velocity measured at the aircraft is the combination of small-scale  
311 turbulence and large-scale vertical motion which cannot be easily disentangled. Roughly 15% of  
312 all plates at high temperatures  $T > -10^{\circ}\text{C}$  are rimed on one side (see Fig. S6a and the corresponding  
313 discussion in the SI) and almost none at lower temperatures. No significant correlation ( $R^2$  below  
314 0.5) or only very minor dependency of riming fraction and CDP droplet number concentration,  
315 CDP mean droplet diameter, ambient vertical velocity, relative cloud height and relative humidity  
316 were found. The corresponding plots are shown in Fig. S3 in the SI.



317 FIG. 6. Three exemplary one-sided, moderately rimed particles shown from different perspectives by the two  
 318 camera telescope assemblies (CTA1 and CTA2). Note that the particle orientation in the stereo image does not  
 319 reflect the actual orientation with respect to horizon.

320 *b. Riming Degree*

321 All rimed ice particles were manually classified concerning their *riming degree*, i.e. their  
 322 estimated surface riming degree. This classification was done manually based on visual inspection  
 323 of the particle's individual stereo-images. Exemplary particles are shown in Fig. 2.

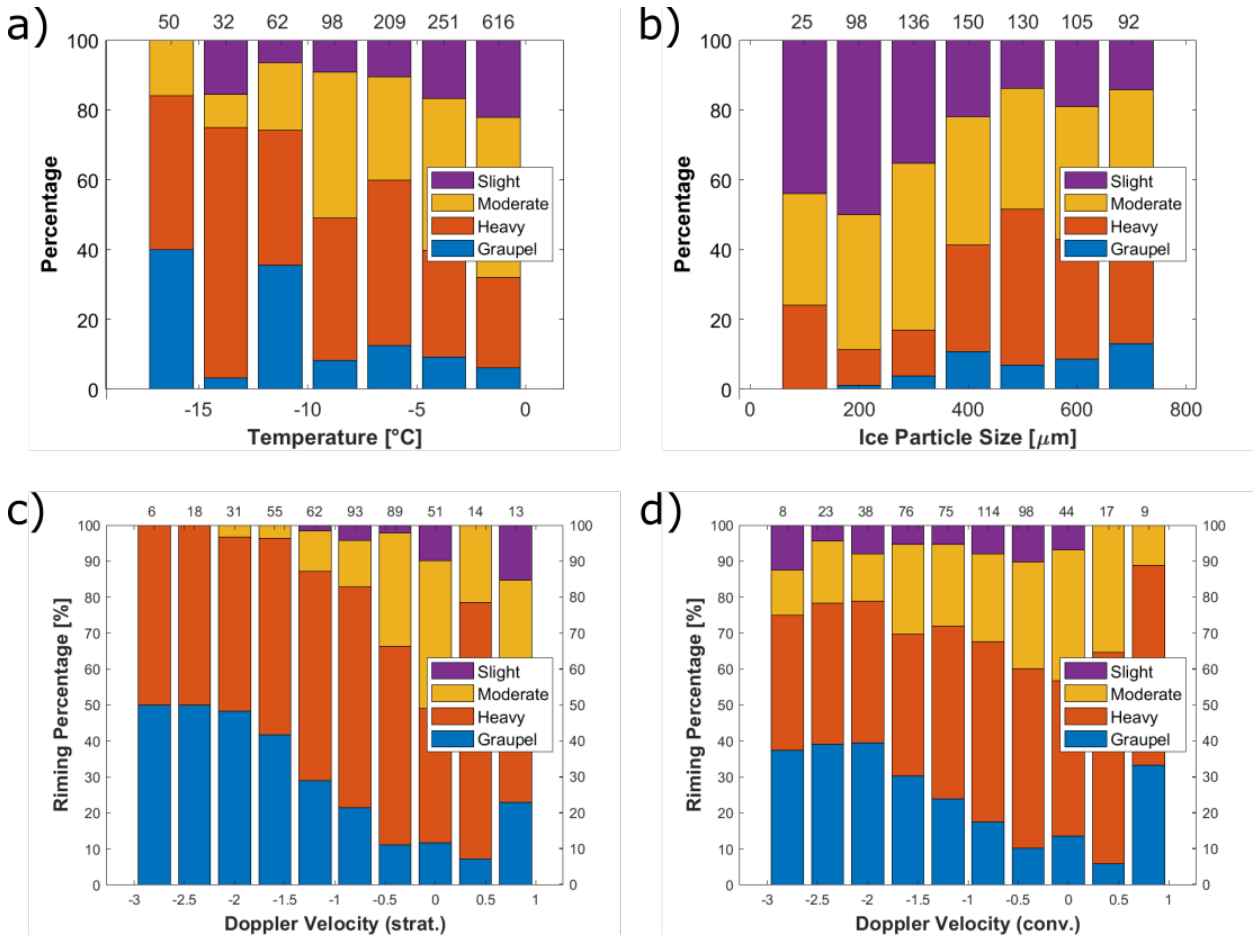
324 Fig. 7 shows the relative distribution of SRD with three ambient and microphysical parameters:  
325 temperature (Fig. 7a), ice particle area equivalent diameter (Fig. 7b) and vertical Doppler velocity  
326 (Fig. 7c). A correlation is seen between temperature and SRD. At lower temperatures ice particles  
327 are more heavily rimed. At temperatures  $T \leq -15^{\circ}\text{C}$ , more than 80% of all rimed particles are  
328 heavily rimed or graupel, whereas most slightly rimed particles are found at high temperatures  
329 between  $-5$  and  $0^{\circ}\text{C}$ .

330 A positive correlation is also visible between SRD and ice particle size: Most small particles  
331 around  $D_{\text{im,A}} \leq 250 \mu\text{m}$  show only slight riming whereas heavy riming is mostly found on larger  
332 particles. These typically large heavily rimed and graupel particles correlate with an increased  
333 negative (downwards) Doppler velocity (Fig. 7c,d) as they are almost spherical and hence more  
334 densely packed compared to aspherical ice particles. This is in agreement with Doppler radar  
335 studies presented by Mosimann (1995). This effect is weaker for convective clouds (Fig. 7d)  
336 compared to stratiform clouds (Fig. 7c). A possible explanation is that the increased fall speed due  
337 to the increase SRD cancels out with updrafts of the air parcels that cause the increased SRD in the  
338 first place. Comparisons with LWC and the other previously discussed parameters (plots shown  
339 in the SI) show no apparent correlation. Since the classification of SRD is only based on visual  
340 inspection, no further numerical analysis was conducted and no fit parameters are presented.

#### 345 4. Epitaxial Riming

346 Rimed ice particles are usually understood as ice particles which have round accretion (rime).  
347 However, during their ageing process, the form of accretion can change significantly. Fig. 8 shows  
348 exemplary rimed ice particles with differently structured rime: round rime (Fig. 8a) and crystalline,  
349 faceted rime (Fig. 8b-e). The latter can be explained by ageing (vapor deposition growth) of rimed  
350 particles. In the following, round rime particles on ice crystal surfaces will be referred to as  
351 "*normal riming*".

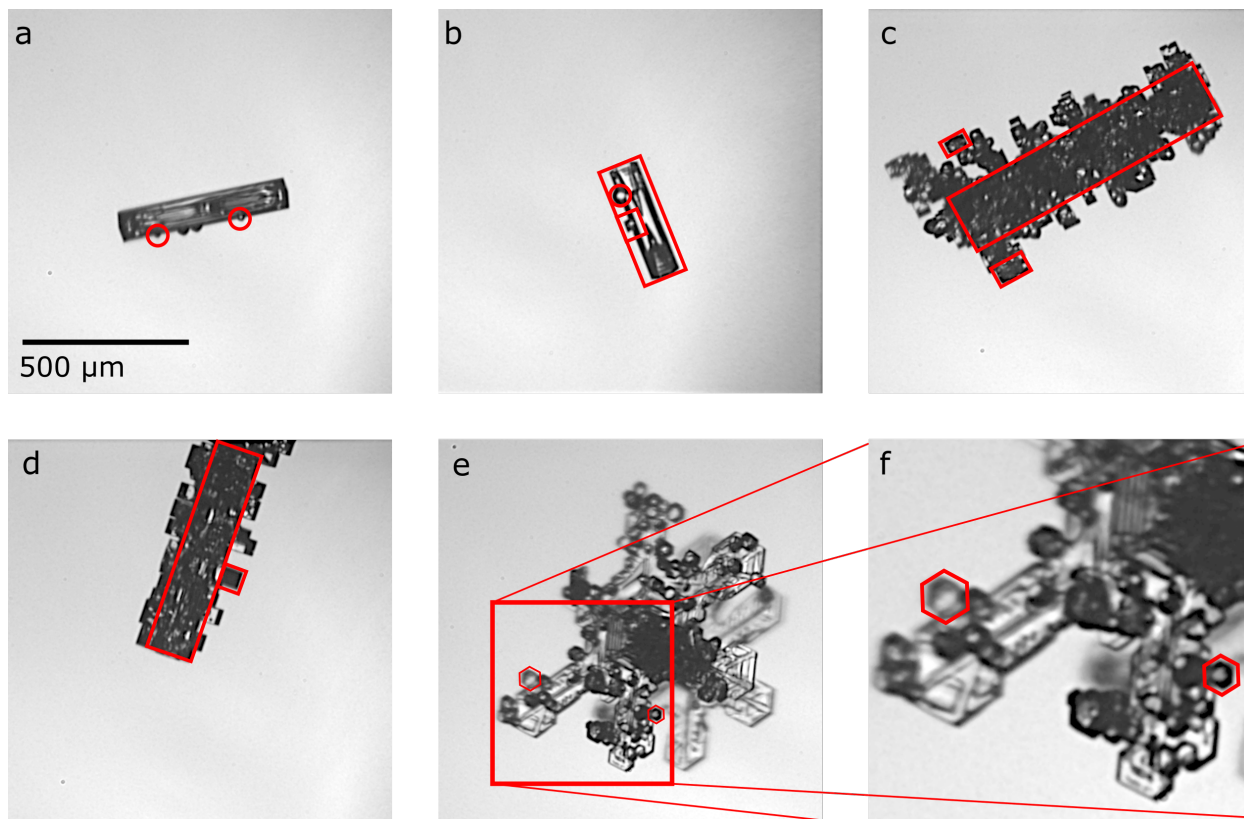
352 Particles with faceted rime have been reported in the past. Korolev et al. (2020) have reported a  
353 case study with "a few ice particles with small faceted particles stuck to their surfaces" which they  
354 refer to as "aged rimed ice particles" that had possibly originated from "vapor deposition regrowth  
355 of rime into faceted particles". Libbrecht (2016) has reported "oriented freezing" of rime particles  
356 that "freeze with their molecular lattices matching the pre-existing lattice underneath" which results



341 FIG. 7. The relative occurrence of particles of different riming degree as defined in Fig. 2: slight (purple),  
 342 moderate (yellow) and heavy riming (red) as well as graupel (blue) in correlation with ambient temperature (a),  
 343 ice particle size (b), and HCR Doppler velocity (c,d) similar to Fig. 4. The values on the upper x-axis correspond  
 344 to the total number of particles per bin.

357 in "faceted rime particles". Since not all aged rimed particles show small faceted particles on the  
 358 surface and the attribute "faceted" is often used in other context for ice particles (pristine plates,  
 359 e.g. Libbrecht et al. (2015); Korolev et al. (2020)), we propose the term "*epitaxial riming*" to  
 360 avoid any confusion. In general, epitaxy refers to crystalline growth of a material on the surface of  
 361 another particle along the lattice structure of the underlying particle (Pashley 1956). The epitaxial  
 362 growth of ice on the surface of crystalline substrates, such as e.g. feldspar, has been the topic of  
 363 many previous works (e.g. Bryant et al. 1960; Kiselev et al. 2016). Here, we describe the growth  
 364 of small ice particles on the surface of larger ice particles along the same crystal axis. Thus, the

365 term "epitaxial riming" refers to faceted, rimed particles, underlining the important property that  
366 the small "rimed" particles on the surface inherit the same lattice structure as the underlying host  
367 particle and share the same c-axis as shown in Fig. 8.



368 FIG. 8. Exemplary rimed ice particles sampled during the IMPACTS campaign: slightly, "normally rimed"  
369 column (a), slightly rimed column with both normal and epitaxial riming (b), heavily epitaxially rimed columns  
370 (c,d) and a moderately, epitaxially rimed plate (e).

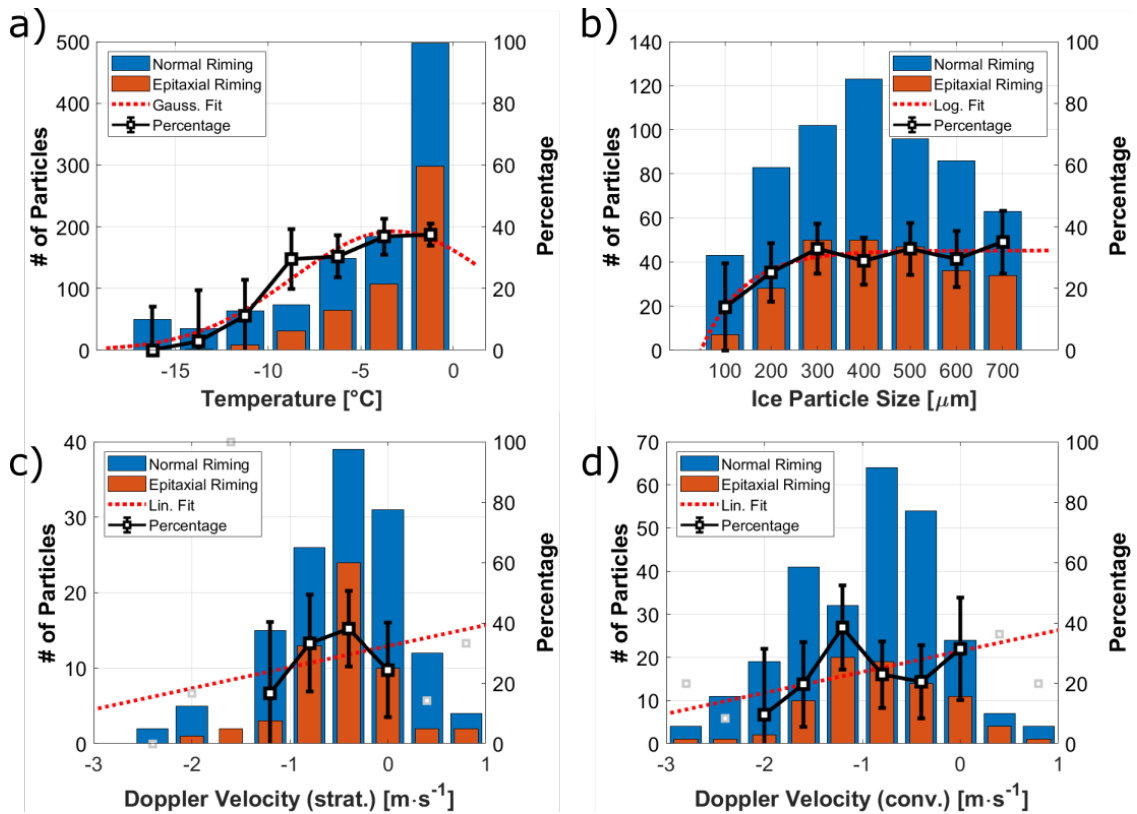
371 Multiple studies exist investigating the orientation of crystallographic axes of the freezing of rime  
372 particles, both in-vitro (Magono and Aburakawa 1969; Takahashi 1979; Mizuno 1984; Mizuno and  
373 Wakahama 1983) and in-situ (Uyeda and Kikuchi 1980). It has been shown that the crystal struc-  
374 ture of rimed (still round) droplets matches the underlying lattice structure. At high temperatures  
375  $-10 \leq T \leq 0^\circ\text{C}$ , most small droplets ( $D \lesssim 40 \mu\text{m}$ ) freeze as single crystals whereas at lower tem-  
376 peratures ( $T \leq -15^\circ\text{C}$ ), rime particles tend to freeze as polycrystals. However, to our knowledge,  
377 so far no studies exist that analyze the properties and formation conditions of the aforementioned



378 epitaxially rimed particles. In the following, we present detailed observations of such ice particles  
 379 and propose that they are the result of vapor deposition on rimed particles.

380 *a. Correlation of Epitaxial Riming with Ambient Conditions*

381 In Fig. 9, we show the relative occurrence of normally and epitaxially rimed particles during the  
 382 ACLOUD and SOCRATES campaign in correlation with ambient microphysical parameters. The  
 383 corresponding fit parameters for all histograms are shown in Tab. 2. Again, only particles sampled  
 384 at a temperature  $T \geq -17^\circ\text{C}$  with diameter  $D \geq 100 \mu\text{m}$  that were distinctively classified according  
 385 to the aforementioned manual classification are included.



386 FIG. 9. Absolute number of analyzed particles for normal (blue) and epitaxial (red) riming and fraction of  
 387 epitaxially rimed particles as a function of ambient temperature (a), ice particle size (b) and HCR Doppler  
 388 velocity for stratiform (c) and convective cloud segments (d). Only bins with more than  $n \geq 20$  data points were  
 389 taken into account ( $n < 20$  are shown in grey).

390 Fig. 9a shows that there is a tendency to find more epitaxial riming at higher temperatures near  
 391  $T = 0^\circ\text{C}$ , where up to almost 40% of all rimed particles show epitaxial riming. Between -5 and



392  $-10^{\circ}\text{C}$ , the fraction of epitaxial riming slightly decreases from 40% to 30%. Below  $T < -10^{\circ}\text{C}$ , the  
 393 percentage of epitaxial riming decreases below 20%, although it should be noted that the statistics  
 394 for this temperature region are weak. This temperature dependency is in accordance with the  
 395 aforementioned studies showing that the rime particles tend to freeze as single crystals along the  
 396 c-axis of the underlying particle.

397 Fig. 9b shows a slight correlation of the occurrence of epitaxial particles with the size of the  
 398 underlying particle. For small particles below  $D \leq 150 \mu\text{m}$ , the fraction of epitaxially rimed  
 399 particles is 20%. This increases to up to 40% for ice particles larger than  $D \geq 300 \mu\text{m}$ . For larger  
 400 particles, the fraction of epitaxially rimed crystals is only weakly dependent of particle size. The  
 401 correlation of particle size with the presence of epitaxial riming can be explained by the fact that  
 402 epitaxial riming is caused by vapor deposition during the ageing process of rimed particles which  
 403 naturally also causes the particle to grow on their main surfaces.

404 Figs. 9c and d show a trend of increasing positive (upward) Doppler velocity with fraction of  
 405 epitaxially rimed particles, indicating a correlation with updrafts. We see no substantial differ-  
 406 ence between the stratiform and convective cases. Again, comparisons with LWC and the other  
 407 previously discussed parameters show no significant correlation (plots shown in the SI).

408 Next, we will present a case study of a MPC sampled during the IMPACTS campaign. We  
 409 investigate the assumption that the ice particles with epitaxial riming are the result of ageing of  
 410 rimed particles and discuss its formation process.

TABLE 2. Fit parameters to the riming percentage histograms shown in Fig. 9.

	Fit function	$R^2$
Temperature	$y = -0.312 x^2 + -1.37 x + 36.6$	0.930
Ice particle diameter (PHIPS)	$y = 32.3 - \exp[-109 (x-367)]$	0.898
Vertical Doppler velocity (HCR, strat.)	$y = 6.98 x + 32.3$	0.144
Vertical Doppler velocity (HCR, conv.)	$y = 6.92 x + 30.7$	0.265

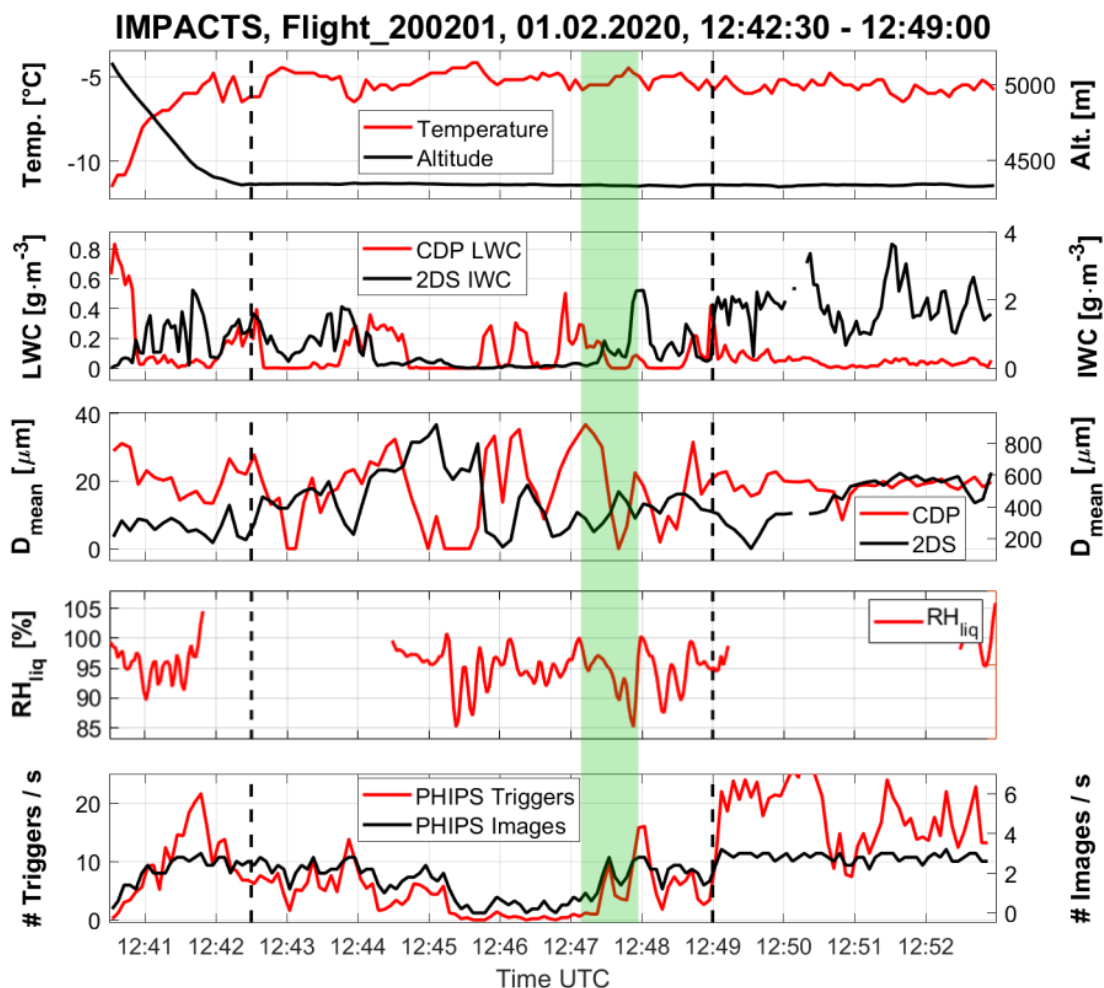
### 411 *b. Case Study Feb01st - Epitaxial Riming on Columns*

412 Fig. 10 shows microphysical data collected on February 1st during the 2020 IMPACTS cam-  
 413 paign. The MPC segment discussed in this case study was probed from 12:42:30 - 12:49:00 UTC  
 414 ( $\Delta t = 06:30$  min, which corresponds to  $\Delta s = 58.5$  km) in an altitude of approximately 4,300 m at  
 415 a temperature of about  $-12^{\circ}\text{C}$  around  $36^{\circ}\text{N}/73^{\circ}\text{W}$ , roughly 300 km near the US east coast. The

416 vertical wind velocity was at a constant value around  $\pm 0 \text{ m s}^{-1}$ . The relative humidity with respect  
417 to water averaged about 93%. The liquid water content (LWC) measured with the CDP averaged  
418 around  $0.1 \text{ g m}^{-3}$  and the total water content (TWC) measured with the 2DS was around  $0.5 \text{ g m}^{-3}$ .  
419 The number-weighted mean particle diameter was around  $20 \mu\text{m}$  for droplets and between 200 to  
420  $800 \mu\text{m}$  for ice particles based on the measurements of CDP and 2D-S, respectively.

421 The trigger threshold of PHIPS was set in a way that the instrument started to trigger on droplets  
422 with diameters larger than  $D > 100 \mu\text{m}$ . In this segment, in total, 1,589 particles were triggered and  
423 575 stereo images were acquired. Examples of micrographs of particles from this flight segment  
424 are shown in Fig. 11. Of the 575 stereo images, 259 (45%) were not classified since they were  
425 identified as potential shattering fragments smaller than  $D = 100 \mu\text{m}$ . Shattering artifacts can be  
426 identified from the PHIPS stereo images that have a field of view of approx.  $2.19 \text{ mm} \times 1.65 \text{ mm}$  by  
427 looking for satellite particles. Even though shattering fragments do not always appear as “satellites”  
428 but can be found as single fragments within the image frame. Such individual shattering fragments  
429 can be typically identified as having sharp edges and a shape that does not appear to resemble  
430 that of a typical vapor grown crystal (i.e. a lack of hexagonal symmetry of the crystal facets). If  
431 such particles were identified during the manual image inspection, they were also categorized as  
432 shattering cases. Of the remaining ice particles (320) most are classified as columnar particles  
433 (173) and 33 as needles. These particles show a wide spectrum of riming degree, ranging from  
434 unrimed (43) to slightly (44), moderately (42) and heavily rimed particles (124). We see different  
435 "types" of riming, most are epitaxially rimed (87), 56 show normal riming. Furthermore, we  
436 see numerous particles with evidence of both normal and epitaxial riming on the same particle  
437 (20), which we refer to as *mixed riming* in the following. Apart from that, we see presence of 3  
438 large drizzle droplets with diameters  $200\text{-}300 \mu\text{m}$  as well as rimed dendrites (30) and graupel (48)  
439 particles. 35 particles were classified as irregulars. Similar particle shapes are observed on the  
440 CPI imagery (not shown here).

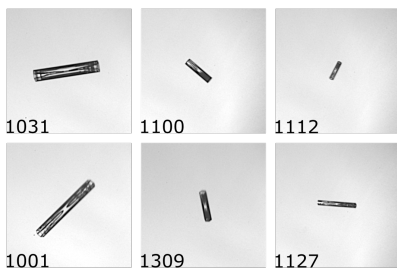
449 The lower panel of Fig. 12 shows four exemplary ice particles that were sampled within a 45 s  
450 window (12:47:07 - 12:47:52 UTC, corresponding to a distance of 6.7 km) that is indicated by the  
451 shaded green area in Fig. 10. The particles that were sampled within this period show columnar  
452 particles during different stages of the riming process: an unrimed (a), a normally rimed (b), a  
453 mixed rimed (c) and epitaxially rimed column (d). Since we observe normal and epitaxial riming



441 FIG. 10. Example of PHIPS data acquired in a mixed-phase cloud near the US east coast sampled during the  
 442 IMPACTS campaign on February 1st, 2020. The graph shows an overview of temperature, altitude, CDP liquid  
 443 water content, 2D-S total water content, CDP and 2D-S number-weighted mean particle diameter and number of  
 444 PHIPS images and total triggers. Corresponding representative PHIPS images of particles sampled during this  
 445 segment are shown in Fig. 11 The green shaded area marks a 45 s segment during which the four particles shown  
 446 in Fig. 12 were acquired.

454 not only within the same segment in near spatial vicinity, but also on the same singular particles,  
 455 we argue that normal and epitaxial riming are, as hypothesized, interlinked. As proposed by  
 456 Korolev et al. (2020), we argue that epitaxial riming is the result of the ageing (deposition growth)  
 457 of normally rimed particles as sketched in the upper panel of Fig. 12: An unrimed ice particle

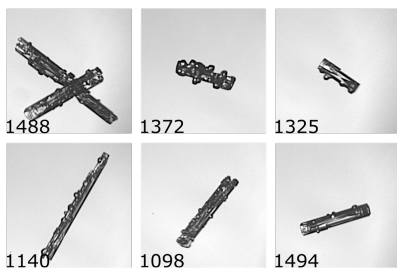
### Unrimed



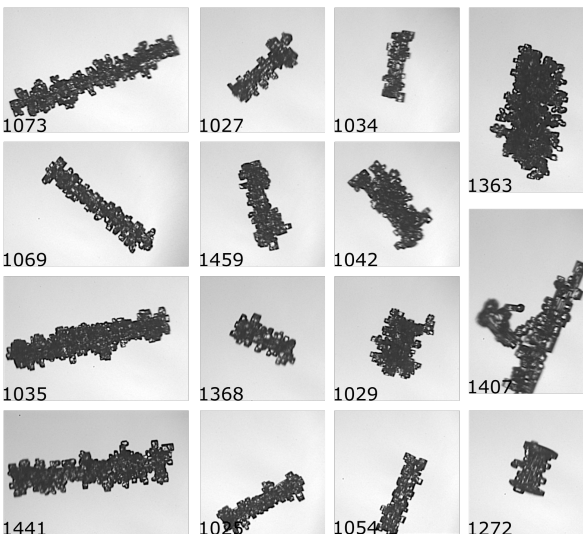
### Slight Epitaxial Rimming



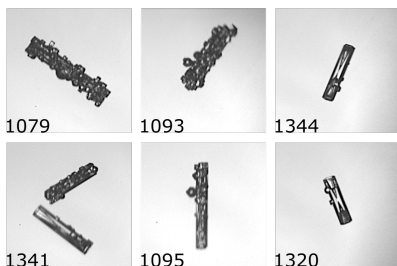
### Normal Rimming



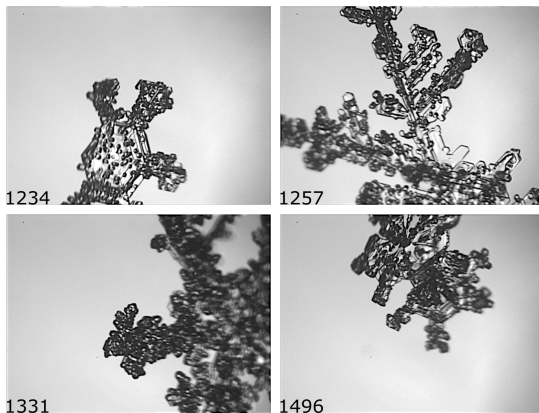
### Heavy Epitaxial Rimming



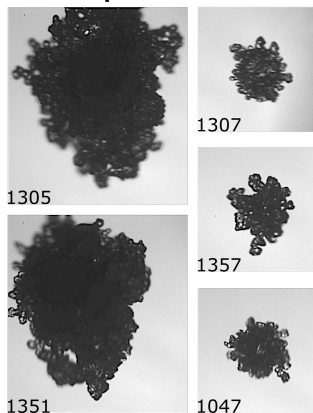
### Mixed



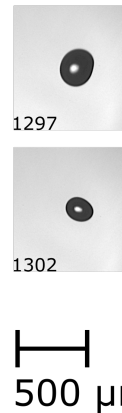
### Rimmed Dendrites



### Graupel



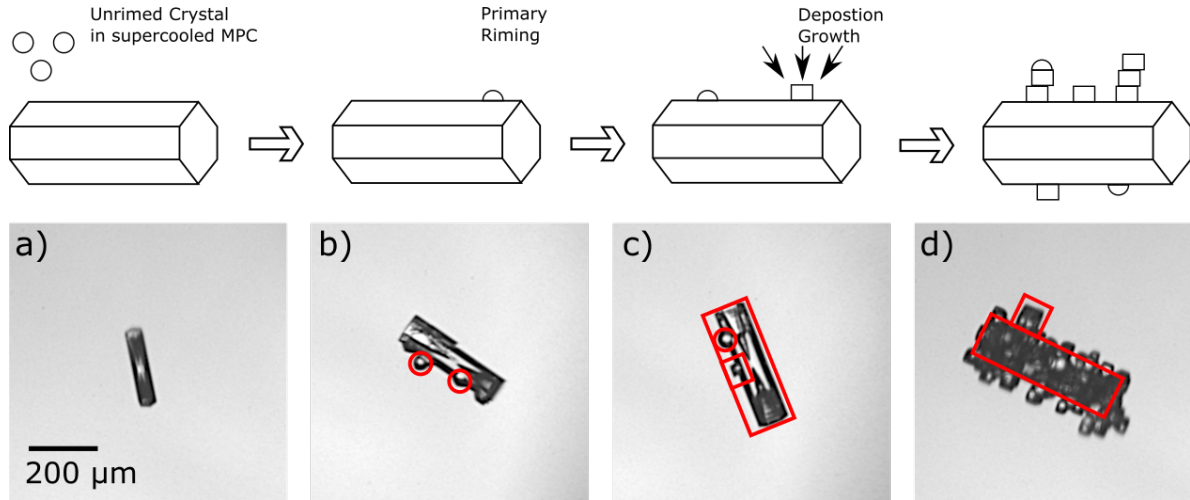
### Drizzle



500  $\mu$ m

447 FIG. 11. Corresponding representative PHIPS images of particles sampled during the segment indicated by  
448 the dashed black lines in in Fig. 10. The numbers in the bottom left denote the image number.

458 (a) accretes a supercooled droplet and forms the initial primary "normal" riming (b). Ambient  
 459 water vapour deposits on the rime matching the lattice structure of the underlying particle and thus  
 460 forming the faceted surface. More droplets are accreted such that normal and epitaxial riming can  
 461 be observed on the same particle (c). The process repeats and the particle grows further until,  
 462 eventually, the whole surface is covered by epitaxial rime (d).



463 FIG. 12. Schematic sketch of an epitaxially rimed column during different stages of the ageing process: unrimed  
 464 (a), normally rimed (b), mixed (c), and epitaxially rimed column (d). The lower panel shows corresponding  
 465 exemplary PHIPS images (#1309, #1325, #1320, and #1368) acquired within a 45 s segment in the presented  
 466 case-study (shaded green area in Fig. 10).

## 467 5. Summary and Conclusion

468 In this work, we have presented in-situ observations using the PHIPS probe during three aircraft  
 469 campaigns targeting MPCs in the Arctic, the Southern Ocean and US east coast. We have shown  
 470 that riming is prevalent in the sampled clouds. We have manually classified ice particles in a  
 471 size range from  $100 \leq D \leq 700 \mu\text{m}$  and in the temperature range between  $-17^\circ\text{C} \leq T \leq 0^\circ\text{C}$  regarding  
 472 their riming status (rimed or unrimed) and surface riming degree (SRD). We show that riming is  
 473 most prevalent at temperatures around  $-7^\circ\text{C}$ , where, on average, 43% of the investigated particles  
 474 showed evidence of riming. We show that riming fraction increases with ice particle size (<20%  
 475 for  $D \leq 200 \mu\text{m}$ , 35-40% for  $D \leq 400 \mu\text{m}$ ) and liquid water content (25% for  $\text{LWC} \leq 0.05 \text{ g m}^{-3}$ , up  
 476 to 60% for  $\text{LWC} = 0.5 \text{ g m}^{-3}$ ).

477 We investigated riming features such as surface riming degree, size of rime particles and one-  
478 sided riming based on visual inspection of individual stereo-images of ice crystals imaged by  
479 PHIPS during these campaigns. We show that the surface riming degree increases with decreasing  
480 temperature and increasing ice particle size.

481 Furthermore, we have described ice particles with faceted, crystalline build-up which is aligned  
482 to the lattice structure of the underlying particle. We call this "epitaxial riming" that we differentiate  
483 from the round "normal riming". Epitaxial riming is most notable in the temperature range from  
484  $-10^{\circ}\text{C} \leq T \leq 0^{\circ}\text{C}$  where epitaxial riming is visible on 32-37% of all rimed particles. We have  
485 presented a case study that demonstrates that normal and epitaxial riming can be observed in  
486 the same cloud segments and even simultaneously on the same single ice particles. We argue  
487 that epitaxially rimed particles are the result of deposition growth of water vapor on primarily  
488 rimed particles during their ageing process. However, further studies are needed to investigate  
489 the exact growth mechanisms of epitaxial riming, for example in laboratory studies. Furthermore,  
490 implications of epitaxial riming are still unclear. For example, it is unclear if epitaxial riming  
491 affects rime splintering process and the splinter production rate.

492 Currently, the implications of riming towards the climate are not yet well understood as most  
493 present day climate prediction models lack a parameterization of riming and consider riming only  
494 for large particles ( $D \geq 1 \text{ mm}$ ) in the sense of graupel and snow. Riming on smaller particles is usu-  
495 ally not considered. The presented correlation between riming fraction and ambient microphysical  
496 parameters can be used as a basis for first steps towards such a riming parameterization for small  
497 or large scale models.

498 *Acknowledgments.* We express our gratitude all participants of the field studies for their efforts,  
499 in particular the technical crew of the AWI Polar 6, NSF G-V and NASA P3. We would like to  
500 acknowledge operational, technical and scientific support provided by NCAR's Earth Observing  
501 Laboratory, sponsored by the National Science Foundation. We thank Ulrike Romatschke for her  
502 valuable help with the HCR data. We would also like to thank the technical and scientific staff of  
503 IMK-AAF for their continuous support. We also thank Alexei Korolev and an anonymous reviewer  
504 who provided valuable feedback that improved and clarified the manuscript. This work  
505 has received funding from the Helmholtz Research Program Atmosphere and Climate, by the

506 German Research Foundation (DFG grants JA 2818/1-1 and SCHN 1140/3-1) and the Helmholtz  
507 Association's Initiative and Networking Fund (grant agreement no. VH-NG-1531).

508 *Data availability statement.* The PHIPS single particle scattering data can be found online in  
509 the PANGAEA database (<https://doi.org/10.1594/PANGAEA.902611>) for ACLOUD and the  
510 EOL database (<https://doi.org/10.5065/D6639NKQ>) for SOCRATES. The single particle  
511 microscopic stereo images from those two campaigns are available upon request from the authors.  
512 The single particle microscopic stereo images from the IMPACTS campaign can be found in the  
513 GHVR DAAC database (<http://dx.doi.org/10.5067/IMPACTS/PHIPS/DATA101>)

## 514 References

515 Abdelmonem, A., E. Järvinen, D. Duft, E. Hirst, S. Vogt, T. Leisner, and M. Schnaiter, 2016:  
516 Phips-halo: the airborne particle habit imaging and polar scattering probe – part 1: Design and  
517 operation. *Atmospheric Measurement Techniques*, **9** (7), 3131–3144, [https://doi.org/10.5194/](https://doi.org/10.5194/amt-9-3131-2016)  
518 [amt-9-3131-2016](https://doi.org/10.5194/amt-9-3131-2016), URL <https://www.atmos-meas-tech.net/9/3131/2016/>.

519 Baltensperger, U., M. Schwikowski, D. Jost, S. Nyeki, H. Gäggeler, and O. Poulida, 1998: Scav-  
520 enging of atmospheric constituents in mixed phase clouds at the high-alpine site jungfrau-  
521 joch part i: Basic concept and aerosol scavenging by clouds. *Atmospheric Environment*,  
522 **32** (23), 3975–3983, [https://doi.org/https://doi.org/10.1016/S1352-2310\(98\)00051-X](https://doi.org/https://doi.org/10.1016/S1352-2310(98)00051-X), URL  
523 <https://www.sciencedirect.com/science/article/pii/S135223109800051X>.

524 Blahak, U., and A. Seifert, 2015: Cosmo / clm / art training course, langen, march 2015. URL  
525 [https://www.hzg.de/imperia/md/assets/clm/neu5\\_tl3.pdf](https://www.hzg.de/imperia/md/assets/clm/neu5_tl3.pdf).

526 Brintjes, R. T., A. J. Heymsfield, and T. W. Krauss, 1987: An examination of double-plate ice crys-  
527 tals and the initiation of precipitation in continental cumulus clouds. *Journal of Atmospheric Sci-*  
528 *ences*, **44** (9), 1331 – 1350, [https://doi.org/10.1175/1520-0469\(1987\)044<1331:AEODPI>2.0.](https://doi.org/10.1175/1520-0469(1987)044<1331:AEODPI>2.0.CO;2)  
529 [CO;2](https://doi.org/10.1175/1520-0469(1987)044<1331:AEODPI>2.0.CO;2), URL [https://journals.ametsoc.org/view/journals/atsc/44/9/1520-0469\\_1987\\_044\\_1331\\_](https://journals.ametsoc.org/view/journals/atsc/44/9/1520-0469_1987_044_1331_aeodpi_2_0_co_2.xml)  
530 [aeodpi\\_2\\_0\\_co\\_2.xml](https://journals.ametsoc.org/view/journals/atsc/44/9/1520-0469_1987_044_1331_aeodpi_2_0_co_2.xml).

531 Bryant, G., J. Hallett, and B. Mason, 1960: The epitaxial growth of ice on single-crystalline  
532 substrates. *Journal of Physics and Chemistry of Solids*, **12** (2), 189–IN18, [https://doi.org/https://doi.org/10.1016/0022-3697\(60\)90018-1](https://doi.org/https://doi.org/10.1016/0022-3697(60)90018-1)

533 //doi.org/10.1016/0022-3697(60)90036-6, URL [https://www.sciencedirect.com/science/article/  
534 pii/0022369760900366](https://www.sciencedirect.com/science/article/pii/0022369760900366).

535 Diao, M., 2021: Vcsel 25hz water vapor data. version 2.0. UCAR/NCAR - Earth Ob-  
536 serving Laboratory, URL <https://data.eol.ucar.edu/dataset/552.052>, [https://doi.org/10.26023/  
537 V925-2H41-SD0F](https://doi.org/10.26023/V925-2H41-SD0F).

538 Ehrlich, A., and Coauthors, 2019: Collection of data sources for the Arctic CLOUD Observations  
539 Using airborne measurements during polar Day (ACLOUD) campaign, North-West of Svalbard  
540 between 23 May - 26 June 2017. PANGAEA, URL <https://doi.org/10.1594/PANGAEA.902603>,  
541 <https://doi.org/10.1594/PANGAEA.902603>.

542 EOL, 2018: Socrates: Southern ocean clouds radiation aerosol transport experimental  
543 study. UCAR/NCAR - Earth Observing Laboratory, URL [https://data.eol.ucar.edu/project/  
544 SOCRATES](https://data.eol.ucar.edu/project/SOCRATES).

545 Fan, J., S. Ghan, M. Ovchinnikov, X. Liu, P. J. Rasch, and A. Korolev, 2011: Rep-  
546 resentation of arctic mixed-phase clouds and the wenger-bergeron-findeisen process in  
547 climate models: Perspectives from a cloud-resolving study. *Journal of Geophysical*  
548 *Research: Atmospheres*, **116 (D1)**, [https://doi.org/https://doi.org/10.1029/2010JD015375](https://doi.org/10.1029/2010JD015375),  
549 URL <https://agupubs.onlinelibrary.wiley.com/doi/abs/10.1029/2010JD015375>, [https://agupubs.  
550 onlinelibrary.wiley.com/doi/pdf/10.1029/2010JD015375](https://agupubs.onlinelibrary.wiley.com/doi/pdf/10.1029/2010JD015375).

551 Field, P. R., and Coauthors, 2017: *Secondary Ice Production - current state of the science and rec-  
552 ommendations for the future*, Meteorological Monographs, Vol. 58, 7.1–7.20. American Mete-  
553 orological Society, Boston (MA), <https://doi.org/10.1175/AMSMONOGRAPHS-D-16-0014.1>,  
554 12.01.01; LK 01.

555 Garrett, T. J., and S. E. Yuter, 2014: Observed influence of riming, temperature, and tur-  
556 bulence on the fallspeed of solid precipitation. *Geophysical Research Letters*, **41 (18)**,  
557 6515–6522, [https://doi.org/https://doi.org/10.1002/2014GL061016](https://doi.org/10.1002/2014GL061016), URL [https://agupubs.  
558 onlinelibrary.wiley.com/doi/abs/10.1002/2014GL061016](https://agupubs.onlinelibrary.wiley.com/doi/abs/10.1002/2014GL061016), [https://agupubs.onlinelibrary.wiley.  
559 com/doi/pdf/10.1002/2014GL061016](https://agupubs.onlinelibrary.wiley.com/doi/pdf/10.1002/2014GL061016).



- 560 Hallett, J., and S. C. Mossop, 1974: Production of secondary ice particles during  
561 the riming process. *Nature*, **249** (5452), 26–28, [https://doi.org/https://doi.org/10.1038/](https://doi.org/https://doi.org/10.1038/249026a0)  
562 249026a0, URL <https://rmets.onlinelibrary.wiley.com/doi/abs/10.1002/qj.49710042514>, <https://rmets.onlinelibrary.wiley.com/doi/pdf/10.1002/qj.49710042514>.
- 564 Harimaya, T., 1975: The riming properties of snow crystals. *Journal of the Meteorological Society of Japan. Ser. II*, **53** (6), 384–392, [https://doi.org/10.2151/jmsj1965.53.6\\_384](https://doi.org/10.2151/jmsj1965.53.6_384).
- 566 Hegg, D. A., A. D. Clarke, S. J. Doherty, and J. Ström, 2011: Measurements of black carbon aerosol  
567 washout ratio on svalbard. *Tellus B*, **63** (5), 891–900, [https://doi.org/https://doi.org/10.1111/](https://doi.org/https://doi.org/10.1111/j.1600-0889.2011.00577.x)  
568 j.1600-0889.2011.00577.x, URL [https://onlinelibrary.wiley.com/doi/abs/10.1111/j.1600-0889.](https://onlinelibrary.wiley.com/doi/abs/10.1111/j.1600-0889.2011.00577.x)  
569 2011.00577.x, <https://onlinelibrary.wiley.com/doi/pdf/10.1111/j.1600-0889.2011.00577.x>.
- 570 Herzegh, P. H., and P. V. Hobbs, 1980: The mesoscale and microscale structure and organization  
571 of clouds and precipitation in midlatitude cyclones. ii: Warm-frontal clouds. *Journal of At-*  
572 *mospheric Sciences*, **37** (3), 597 – 611, [https://doi.org/10.1175/1520-0469\(1980\)037<0597:](https://doi.org/10.1175/1520-0469(1980)037<0597:TMAMSA>2.0.CO;2)  
573 [TMAMSA>2.0.CO;2](https://doi.org/10.1175/1520-0469(1980)037<0597:TMAMSA>2.0.CO;2), URL [https://journals.ametsoc.org/view/journals/atsc/37/3/1520-0469\\_](https://journals.ametsoc.org/view/journals/atsc/37/3/1520-0469_1980_037_0597_tmamsa_2_0_co_2.xml)  
574 [1980\\_037\\_0597\\_tmamsa\\_2\\_0\\_co\\_2.xml](https://journals.ametsoc.org/view/journals/atsc/37/3/1520-0469_1980_037_0597_tmamsa_2_0_co_2.xml).
- 575 Järvinen, E., and Coauthors, 2018: Additional global climate cooling by clouds due to ice crystal  
576 complexity. *Atmospheric Chemistry and Physics*, **18** (21), 15 767–15 781, [https://doi.org/10.](https://doi.org/10.5194/acp-18-15767-2018)  
577 [5194/acp-18-15767-2018](https://doi.org/10.5194/acp-18-15767-2018), URL <https://www.atmos-chem-phys.net/18/15767/2018/>.
- 578 Järvinen, E., and Coauthors, 2021: Ice crystal complexity and link to cirrus cloud radiative effect.  
579 *Journal of Geophysical Research: Atmospheres*, **2021**, in review.
- 580 Keppas, S. C., J. Crosier, T. W. Choularton, and K. N. Bower, 2017: Ice lollies: An ice  
581 particle generated in supercooled conveyor belts. *Geophysical Research Letters*, **44** (10),  
582 5222–5230, <https://doi.org/https://doi.org/10.1002/2017GL073441>, URL [https://agupubs.](https://agupubs.onlinelibrary.wiley.com/doi/abs/10.1002/2017GL073441)  
583 [onlinelibrary.wiley.com/doi/abs/10.1002/2017GL073441](https://agupubs.onlinelibrary.wiley.com/doi/abs/10.1002/2017GL073441), [https://agupubs.onlinelibrary.wiley.](https://agupubs.onlinelibrary.wiley.com/doi/pdf/10.1002/2017GL073441)  
584 [com/doi/pdf/10.1002/2017GL073441](https://agupubs.onlinelibrary.wiley.com/doi/pdf/10.1002/2017GL073441).
- 585 Khain, A., A. Pokrovsky, and I. Sednev, 1999: Some effects of cloud–aerosol interaction on cloud  
586 microphysics structure and precipitation formation: numerical experiments with a spectral

587 microphysics cloud ensemble model. *Atmospheric Research*, **52** (3), 195–220, [https://doi.org/](https://doi.org/https://doi.org/10.1016/S0169-8095(99)00027-7)  
588 [https://doi.org/10.1016/S0169-8095\(99\)00027-7](https://doi.org/10.1016/S0169-8095(99)00027-7), URL [https://www.sciencedirect.com/science/](https://www.sciencedirect.com/science/article/pii/S0169809599000277)  
589 [article/pii/S0169809599000277](https://www.sciencedirect.com/science/article/pii/S0169809599000277).

590 Kikuchi, K., and H. Uyeda, 1979: Cloud droplets and rain drops collected and frozen on nat-  
591 ural snow crystals. *Journal of the Meteorological Society of Japan. Ser. II*, **57** (3), 273–281,  
592 [https://doi.org/10.2151/jmsj1965.57.3\\_273](https://doi.org/10.2151/jmsj1965.57.3_273).

593 Kiselev, A., F. Bachmann, P. Pedevilla, S. J. Cox, A. Michaelides, D. Gerthsen, and T. Leisner,  
594 2016: Active sites in heterogeneous ice nucleation—the example of k-rich feldspars. *Science*,  
595 <https://doi.org/10.1126/science.aai8034>, URL [https://science.sciencemag.org/content/early/](https://science.sciencemag.org/content/early/2016/12/07/science.aai8034)  
596 [2016/12/07/science.aai8034](https://science.sciencemag.org/content/early/2016/12/07/science.aai8034), [https://science.sciencemag.org/content/early/2016/12/07/science.](https://science.sciencemag.org/content/early/2016/12/07/science.aai8034.full.pdf)  
597 [aai8034.full.pdf](https://science.sciencemag.org/content/early/2016/12/07/science.aai8034.full.pdf).

598 Kneifel, S., and D. Moisseev, 2020: Long-term statistics of riming in nonconvective clouds derived  
599 from ground-based doppler cloud radar observations. *Journal of the Atmospheric Sciences*,  
600 **77** (10), 3495 – 3508, <https://doi.org/10.1175/JAS-D-20-0007.1>, URL [https://journals.ametsoc.](https://journals.ametsoc.org/view/journals/atsc/77/10/jasD200007.xml)  
601 [org/view/journals/atsc/77/10/jasD200007.xml](https://journals.ametsoc.org/view/journals/atsc/77/10/jasD200007.xml).

602 Knudsen, E. M., and Coauthors, 2018: Meteorological conditions during the acloud/pascal  
603 field campaign near svalbard in early summer 2017. *Atmospheric Chemistry and Physics*,  
604 **18** (24), 17 995–18 022, <https://doi.org/10.5194/acp-18-17995-2018>, URL [https://www.](https://www.atmos-chem-phys.net/18/17995/2018/)  
605 [atmos-chem-phys.net/18/17995/2018/](https://www.atmos-chem-phys.net/18/17995/2018/).

606 Korolev, A., and Coauthors, 2017: Mixed-phase clouds: Progress and challenges. *Meteoro-*  
607 *logical Monographs*, **58**, 5.1–5.50, [https://doi.org/10.1175/AMSMONOGRAPHS-D-17-0001.](https://doi.org/10.1175/AMSMONOGRAPHS-D-17-0001.1)  
608 [1](https://doi.org/10.1175/AMSMONOGRAPHS-D-17-0001.1), URL [https://doi.org/10.1175/](https://doi.org/10.1175/AMSMONOGRAPHS-D-17-0001.1)  
609 [AMSMONOGRAPHS-D-17-0001.1](https://doi.org/10.1175/AMSMONOGRAPHS-D-17-0001.1).

610 Korolev, A., and Coauthors, 2020: A new look at the environmental conditions favorable to sec-  
611 ondary ice production. *Atmospheric Chemistry and Physics*, **20** (3), 1391–1429, [https://doi.org/](https://doi.org/10.5194/acp-20-1391-2020)  
612 [10.5194/acp-20-1391-2020](https://doi.org/10.5194/acp-20-1391-2020), URL <https://acp.copernicus.org/articles/20/1391/2020/>.

613 Leinonen, J., and W. Szyrmer, 2015: Radar signatures of snowflake riming: A  
614 modeling study. *Earth and Space Science*, **2** (8), 346–358, [https://doi.org/https://doi.](https://doi.org/https://doi.org/10.1002/2015EA000277)

615 org/10.1002/2015EA000102, URL [https://agupubs.onlinelibrary.wiley.com/doi/abs/10.1002/](https://agupubs.onlinelibrary.wiley.com/doi/abs/10.1002/2015EA000102)  
616 2015EA000102, <https://agupubs.onlinelibrary.wiley.com/doi/pdf/10.1002/2015EA000102>.

617 Leinonen, J., and Coauthors, 2018: Retrieval of snowflake microphysical properties from mul-  
618 tiframe radar observations. *Atmospheric Measurement Techniques*, **11** (10), 5471–5488,  
619 <https://doi.org/10.5194/amt-11-5471-2018>, URL [https://amt.copernicus.org/articles/11/5471/](https://amt.copernicus.org/articles/11/5471/2018/)  
620 2018/.

621 Libbrecht, K., 2016: *Ken Libbrecht's Field Guide to Snowflakes*. Voyageur Press, URL [https://](https://books.google.de/books?id=eOv83aUgOvwC)  
622 [books.google.de/books?id=eOv83aUgOvwC](https://books.google.de/books?id=eOv83aUgOvwC).

623 Libbrecht, K., C. Miller, R. Potter, N. Budaeva, C. Lemon, and S. Thomas, 2015: Toward a  
624 comprehensive model of snow crystal growth: 4. measurements of diffusion-limited growth at  
625 -15 c.

626 Lin, Y., L. Donner, and B. Colle, 2011: Parameterization of riming intensity and its impact on ice  
627 fall speed using arm data. *Monthly Weather Review - MON WEATHER REV*, **139**, 1036–1047,  
628 <https://doi.org/10.1175/2010MWR3299.1>.

629 Locatelli, J. D., and P. V. Hobbs, 1974: Fall speeds and masses of solid precipitation  
630 particles. *Journal of Geophysical Research (1896-1977)*, **79** (15), 2185–2197, [https://doi.org/](https://doi.org/https://doi.org/10.1029/JC079i015p02185)  
631 <https://doi.org/10.1029/JC079i015p02185>, URL [https://agupubs.onlinelibrary.wiley.com/doi/](https://agupubs.onlinelibrary.wiley.com/doi/abs/10.1029/JC079i015p02185)  
632 [abs/10.1029/JC079i015p02185](https://doi.org/10.1029/JC079i015p02185), [https://agupubs.onlinelibrary.wiley.com/doi/pdf/10.1029/](https://agupubs.onlinelibrary.wiley.com/doi/pdf/10.1029/JC079i015p02185)  
633 [JC079i015p02185](https://doi.org/10.1029/JC079i015p02185).

634 Magono, C., and H. Aburakawa, 1969: Experimental studies on snow crystals of plane type with  
635 spatial branches. *Journal of the Faculty of Science, Hokkaido University. Series 7, Geophysics*,  
636 **3** (2), 85–97, URL <http://hdl.handle.net/2115/8680>.

637 Magono, C., and C. W. Lee, 1966: Meteorological classification of natural snow crystals. *Journal*  
638 *of the Faculty of Science, Hokkaido University. Series 7, Geophysics*, **2** (4), 321–335, URL  
639 <http://hdl.handle.net/2115/8672>.

640 Martin, M. Y., and R. Bennett, 2020: P-3 meteorological and navigation data impacts. NASA  
641 Global Hydrometeorology Resource Center DAAC, URL [https://ghrc.nsstc.nasa.gov/hydro/](https://ghrc.nsstc.nasa.gov/hydro/details/p3metnavimpacts)  
642 [details/p3metnavimpacts](https://doi.org/10.5067/IMPACTS/P3/DATA101), <https://doi.org/10.5067/IMPACTS/P3/DATA101>.

643 Mason, S. L., C. J. Chiu, R. J. Hogan, D. Moisseev, and S. Kneifel, 2018: Retrievals of riming  
644 and snow density from vertically pointing doppler radars. *Journal of Geophysical Research:*  
645 *Atmospheres*, **123** (24), 13,807–13,834, [https://doi.org/https://doi.org/10.1029/2018JD028603](https://doi.org/10.1029/2018JD028603),  
646 URL <https://agupubs.onlinelibrary.wiley.com/doi/abs/10.1029/2018JD028603>, <https://agupubs.onlinelibrary.wiley.com/doi/pdf/10.1029/2018JD028603>.

648 McCoy, D. T., I. Tan, D. L. Hartmann, M. D. Zelinka, and T. Storelvmo,  
649 2016: On the relationships among cloud cover, mixed-phase partitioning, and  
650 planetary albedo in gcms. *Journal of Advances in Modeling Earth Systems*,  
651 **8** (2), 650–668, <https://doi.org/10.1002/2015MS000589>, URL <https://agupubs.onlinelibrary.wiley.com/doi/abs/10.1002/2015MS000589>, <https://agupubs.onlinelibrary.wiley.com/doi/pdf/10.1002/2015MS000589>.

654 McFarquhar, G. M., and Coauthors, 2019: Airborne, ship-, and ground-based observations of  
655 clouds, aerosols, and precipitation from recent field projects over the southern ocean. *99th annual meeting, American Meteorological Society*, URL <https://ams.confex.com/ams/2019Annual/meetingapp.cgi/Paper/350863>.

658 McMurdie, L., G. Heymsfield, J. Yorks, and S. Braun, 2019: Investigation of microphysics and  
659 precipitation for atlantic coast-threatening snowstorms (impacts) collection. NASA EOSDIS  
660 Global Hydrology Resource Center Distributed, Active Archive Center, Huntsville, Alabama,  
661 U.S.A., URL <http://dx.doi.org/10.5067/IMPACTS/DATA101>.

662 Mizuno, Y., 1984: Epitaxial freezing of supercooled droplets on ice surfaces. *Contributions from*  
663 *the Institute of Low Temperature Science*, **A33**, 1–27, URL <http://hdl.handle.net/2115/20248>.

664 Mizuno, Y., and G. Wakahama, 1983: Structure and orientation of frozen droplets on ice surfaces.  
665 *The Journal of Physical Chemistry*, **87** (21), 4161–4167, <https://doi.org/10.1021/j100244a037>,  
666 URL <https://doi.org/10.1021/j100244a037>, <https://doi.org/10.1021/j100244a037>.

667 Mosimann, L., 1995: An improved method for determining the degree of snow crystal  
668 riming by vertical doppler radar. *Atmospheric Research*, **37** (4), 305–323, [https://doi.org/https://doi.org/10.1016/0169-8095\(94\)00050-N](https://doi.org/10.1016/0169-8095(94)00050-N), URL <https://www.sciencedirect.com/science/article/pii/016980959400050N>.

671 Mosimann, L., M. Steiner, J. Collett, and et al., 1993: Ice crystal observations and the degree  
672 of riming in winter precipitation. *Water Air Soil Pollution*, **68**, 29–42, <https://doi.org/https://doi.org/10.1007/BF00479391>.

674 Mosimann, L., E. Weingartner, and A. Waldvogel, 1994: An analysis of accreted  
675 drop sizes and mass on rimed snow crystals. *Journal of Atmospheric Sciences*,  
676 **51 (11)**, 1548 – 1558, [https://doi.org/10.1175/1520-0469\(1994\)051<1548:AAOADS>2.0.CO;](https://doi.org/10.1175/1520-0469(1994)051<1548:AAOADS>2.0.CO;2)  
677 2, URL [https://journals.ametsoc.org/view/journals/atsc/51/11/1520-0469\\_1994\\_051\\_1548\\_](https://journals.ametsoc.org/view/journals/atsc/51/11/1520-0469_1994_051_1548_aaoads_2_0_co_2.xml)  
678 [aaoads\\_2\\_0\\_co\\_2.xml](https://journals.ametsoc.org/view/journals/atsc/51/11/1520-0469_1994_051_1548_aaoads_2_0_co_2.xml).

679 Ono, A., 1969: The shape and riming properties of ice crystals in natural clouds. *Journal of At-*  
680 *mospheric Sciences*, **26 (1)**, 138 – 147, [https://doi.org/10.1175/1520-0469\(1969\)026<0138:](https://doi.org/10.1175/1520-0469(1969)026<0138:TSARPO>2.0.CO;2)  
681 [TSARPO>2.0.CO;2](https://doi.org/10.1175/1520-0469(1969)026<0138:TSARPO>2.0.CO;2), URL [https://journals.ametsoc.org/view/journals/atsc/26/1/1520-0469\\_](https://journals.ametsoc.org/view/journals/atsc/26/1/1520-0469_1969_026_0138_tsarpo_2_0_co_2.xml)  
682 [1969\\_026\\_0138\\_tsarpo\\_2\\_0\\_co\\_2.xml](https://journals.ametsoc.org/view/journals/atsc/26/1/1520-0469_1969_026_0138_tsarpo_2_0_co_2.xml).

683 Ovchinnikov, M., and Coauthors, 2014: Intercomparison of large-eddy simulations of  
684 arctic mixed-phase clouds: Importance of ice size distribution assumptions. *Jour-*  
685 *nal of Advances in Modeling Earth Systems*, **6 (1)**, 223–248, [https://doi.org/https://doi.](https://doi.org/https://doi.org/10.1002/2013MS000282)  
686 [org/10.1002/2013MS000282](https://doi.org/10.1002/2013MS000282), URL [https://agupubs.onlinelibrary.wiley.com/doi/abs/10.1002/](https://agupubs.onlinelibrary.wiley.com/doi/abs/10.1002/2013MS000282)  
687 [2013MS000282](https://agupubs.onlinelibrary.wiley.com/doi/pdf/10.1002/2013MS000282), <https://agupubs.onlinelibrary.wiley.com/doi/pdf/10.1002/2013MS000282>.

688 Pashley, D., 1956: The study of epitaxy in thin surface films. *Advances in Physics*,  
689 **5 (18)**, 173–240, <https://doi.org/10.1080/00018735600101175>, URL [https://doi.org/10.1080/](https://doi.org/10.1080/00018735600101175)  
690 [00018735600101175](https://doi.org/10.1080/00018735600101175), <https://doi.org/10.1080/00018735600101175>.

691 Pflaum, J. C., and H. R. Pruppacher, 1979: A wind tunnel investigation of the growth of  
692 graupel initiated from frozen drops. *Journal of Atmospheric Sciences*, **36 (4)**, 680 – 689,  
693 [https://doi.org/10.1175/1520-0469\(1979\)036<0680:AWTIOT>2.0.CO;2](https://doi.org/10.1175/1520-0469(1979)036<0680:AWTIOT>2.0.CO;2), URL [https://journals.](https://journals.ametsoc.org/view/journals/atsc/36/4/1520-0469_1979_036_0680_awtiot_2_0_co_2.xml)  
694 [ametsoc.org/view/journals/atsc/36/4/1520-0469\\_1979\\_036\\_0680\\_awtiot\\_2\\_0\\_co\\_2.xml](https://journals.ametsoc.org/view/journals/atsc/36/4/1520-0469_1979_036_0680_awtiot_2_0_co_2.xml).

695 Rango, A., J. Foster, E. G. Josberger, E. F. Erbe, W. P. Wergin, and C. Pooley, 2003:  
696 Rime and graupel: Description and characterization as revealed by low-temperature scan-  
697 ning electron microscopy. *Scanning*, **25 (3)**, 121–131, [https://doi.org/https://doi.org/10.1002/](https://doi.org/https://doi.org/10.1002/sca.4950250304)  
698 [sca.4950250304](https://doi.org/10.1002/sca.4950250304), URL <https://onlinelibrary.wiley.com/doi/abs/10.1002/sca.4950250304>, <https://onlinelibrary.wiley.com/doi/pdf/10.1002/sca.4950250304>.

- 700 Romatschke, U., 2021: Melting layer detection and observation with the near airborne w-band  
701 radar. *Remote Sensing*, **13** (9), <https://doi.org/10.3390/rs13091660>, URL <https://www.mdpi.com/2072-4292/13/9/1660>.  
702
- 703 Romatschke, U., and M. Dixon, 2022: Vertically resolved convective/stratiform echo type identifi-  
704 cation and convectivity retrieval for vertically pointing radars. <https://doi.org/10.31223/x54s77>,  
705 URL <https://doi.org/10.31223/x54s77>.
- 706 Saleeby, S. M., and W. R. Cotton, 2008: A binned approach to cloud-droplet riming imple-  
707 mented in a bulk microphysics model. *Journal of Applied Meteorology and Climatology*, **47** (2),  
708 694 – 703, <https://doi.org/10.1175/2007JAMC1664.1>, URL [https://journals.ametsoc.org/view/](https://journals.ametsoc.org/view/journals/apme/47/2/2007jamc1664.1.xml)  
709 [journals/apme/47/2/2007jamc1664.1.xml](https://journals/apme/47/2/2007jamc1664.1.xml).
- 710 Schnaiter, M., E. Järvinen, A. Abdelmonem, and T. Leisner, 2018: Phips-halo: the airborne parti-  
711 cle habit imaging and polar scattering probe – part 2: Characterization and first results. *Atmo-  
712 spheric Measurement Techniques*, **11** (1), 341–357, <https://doi.org/10.5194/amt-11-341-2018>,  
713 URL <https://www.atmos-meas-tech.net/11/341/2018/>.
- 714 Schnaiter, M., and Coauthors, 2016: Cloud chamber experiments on the origin of ice crystal com-  
715 plexity in cirrus clouds. *Atmospheric Chemistry and Physics*, **16** (8), 5091–5110, [https://doi.org/](https://doi.org/10.5194/acp-16-5091-2016)  
716 [10.5194/acp-16-5091-2016](https://doi.org/10.5194/acp-16-5091-2016), URL <https://acp.copernicus.org/articles/16/5091/2016/>.
- 717 Schön, R., and Coauthors, 2011: Particle habit imaging using incoherent light: A first step toward  
718 a novel instrument for cloud microphysics. *Journal of Atmospheric and Oceanic Technology*,  
719 **28** (4), 493–512, <https://doi.org/10.1175/2011JTECHA1445.1>, URL [https://doi.org/10.1175/](https://doi.org/10.1175/2011JTECHA1445.1)  
720 [2011JTECHA1445.1](https://doi.org/10.1175/2011JTECHA1445.1), <https://doi.org/10.1175/2011JTECHA1445.1>.
- 721 Stevens, R. G., and Coauthors, 2018: A model intercomparison of ccn-limited tenuous clouds in  
722 the high arctic. *Atmospheric Chemistry and Physics*, **18** (15), 11 041–11 071, [https://doi.org/](https://doi.org/10.5194/acp-18-11041-2018)  
723 [10.5194/acp-18-11041-2018](https://doi.org/10.5194/acp-18-11041-2018), URL <https://acp.copernicus.org/articles/18/11041/2018/>.
- 724 Takahashi, C., 1979: Formation of poly-crystalline snow crystals by riming process. *Journal of the  
725 Meteorological Society of Japan. Ser. II*, **57** (5), 458–464, [https://doi.org/10.2151/jmsj1965.57.](https://doi.org/10.2151/jmsj1965.57.5_458)  
726 [5\\_458](https://doi.org/10.2151/jmsj1965.57.5_458).

- 727 UCAR/NCAR-Earth Observing Laboratory, 2019: Socrates: Low rate (lrt - 1 sps) navigation, state  
728 parameter, and microphysics flight-level data. version 1.3. UCAR/NCAR - Earth Observing Lab-  
729 oratory, URL <https://data.eol.ucar.edu/dataset/552.002>, <https://doi.org/10.5065/D6M32TM9>.
- 730 UCAR/NCAR-EOL, 2022: Ncar hcr radar and hsrl lidar moments data. version 3.0. ucar/ncar -  
731 earth observing laboratory. URL <https://doi.org/10.5065/D68914PH>.
- 732 Uyeda, H., and K. Kikuchi, 1978: Freezing experiment of supercooled water droplets frozen by  
733 using single crystal ice. *Journal of the Meteorological Society of Japan. Ser. II*, **56** (1), 43–51,  
734 [https://doi.org/10.2151/jmsj1965.56.1\\_43](https://doi.org/10.2151/jmsj1965.56.1_43).
- 735 Uyeda, H., and K. Kikuchi, 1980: Measurements of the principal axis of frozen hemispheric water  
736 droplets. *Journal of the Meteorological Society of Japan. Ser. II*, **58** (1), 52–58, [https://doi.org/10.2151/jmsj1965.58.1\\_52](https://doi.org/10.2151/jmsj1965.58.1_52).
- 737
- 738 Waitz, F., M. Schnaiter, T. Leisner, and E. Järvinen, 2021: Phips-halo: the airborne particle habit  
739 imaging and polar scattering probe – part 3: Single particle phase discrimination and particle  
740 size distribution based on angular scattering function. *Atmospheric Measurement Techniques*  
741 *Discussions*, **2021**, 1–28, <https://doi.org/10.5194/amt-2020-297>, URL <https://amt.copernicus.org/preprints/amt-2020-297/>.
- 742
- 743 Wang, P. K., and W. Ji, 2000: Collision efficiencies of ice crystals at low–intermediate reynolds  
744 numbers colliding with supercooled cloud droplets: A numerical study. *Journal of the At-*  
745 *mospheric Sciences*, **57** (8), 1001 – 1009, [https://doi.org/10.1175/1520-0469\(2000\)057<1001:](https://doi.org/10.1175/1520-0469(2000)057<1001:CEOICA>2.0.CO;2)  
746 [CEOICA>2.0.CO;2](https://doi.org/10.1175/1520-0469(2000)057<1001:CEOICA>2.0.CO;2), URL [https://journals.ametsoc.org/view/journals/atsc/57/8/1520-0469\\_](https://journals.ametsoc.org/view/journals/atsc/57/8/1520-0469_2000_057_1001_ceoica_2.0.co_2.xml)  
747 [2000\\_057\\_1001\\_ceoica\\_2.0.co\\_2.xml](https://journals.ametsoc.org/view/journals/atsc/57/8/1520-0469_2000_057_1001_ceoica_2.0.co_2.xml).
- 748 Wendisch, M., A. Macke, A. Ehrlich, C. Lüpkes, and Coauthors, 2019: The arctic cloud puzzle:  
749 Using acloud/pascal multiplatform observations to unravel the role of clouds and aerosol particles  
750 in arctic amplification. *Bulletin of the American Meteorological Society*, **100** (5), 841–871,  
751 <https://doi.org/10.1175/BAMS-D-18-0072.1>, URL [https://doi.org/10.1175/BAMS-D-18-0072.](https://doi.org/10.1175/BAMS-D-18-0072.1)  
752 [1](https://doi.org/10.1175/BAMS-D-18-0072.1), <https://doi.org/10.1175/BAMS-D-18-0072.1>.
- 753 Ávila, E. E., N. E. Castellano, C. P. R. Saunders, R. E. Bürgesser, and G. G. Aguirre Varela,  
754 2009: Initial stages of the riming process on ice crystals. *Geophysical Research Let-*

755 *ters*, **36 (9)**, <https://doi.org/https://doi.org/10.1029/2009GL037723>, URL <https://agupubs.onlinelibrary.wiley.com/doi/abs/10.1029/2009GL037723>,  
756 <https://agupubs.onlinelibrary.wiley.com/doi/pdf/10.1029/2009GL037723>.  
757